

DESIGN AND DEVELOPMENT OF A HYBRID RENEWABLE ENERGY SYSTEM USING FUZZY LOGIC CONTROLLER FOR MAXIMUM POWER POINT TRACKING

日隈, 龍也
九州大学総合理工学府環境エネルギー工学専攻

<https://hdl.handle.net/2324/4372236>

出版情報 : 九州大学, 2020, 修士, 修士
バージョン :
権利関係 :

DESIGN AND DEVELOPMENT OF A HYBRID RENEWABLE ENERGY SYSTEM USING FUZZY LOGIC CONTROLLER FOR MAXIMUM POWER POINT TRACKING

Tatsuya Hinokuma

Supervisor

Associate Professor. Hooman Farzaneh



February 2021

Energy and Environmental System Laboratory,
Department of Energy and Environmental Engineering
Interdisciplinary Graduate School of Engineering
Sciences

KYUSHU UNIVERSITY
Japan

CONTENTS

ABSTRACT.....	5
ACKNOWLEDGMENT.....	6
CHAPTER 1: INTRODUCTION.....	7
1.1. ENERGY SITUATION IN JAPAN.....	7
1.2. FUTURE PLANS OF THE RENEWABLE ENERGY SYSTEM IN JAPAN.....	8
1.3. HYBRID RENEWABLE ENERGY SYSTEM.....	9
1.4. WHAT WILL BE ELUCIDATED IN THIS RESEARCH.....	10
CHAPTER 2: FUNDAMENTAL OF THE SOLAR AND WIND POWER GENERATION.....	12
2.1. PRINCIPLE OF POWER GENERATION BY THE SOLAR CELL.....	12
2.1.1. EQUIVALENT ELECTRIC CIRCUIT OF A SOLAR CELL.....	12
2.1.2. PV CHARACTERISTIC CURVE.....	14
2.2. FUNDAMENTAL OF THE WIND POWER GENERATOR.....	16
2.2.1. PERMANENT MAGNET SYNCHRONOUS GENERATOR (PMSG).....	18
2.2.2. RECTIFIER.....	20
2.3. OUTPUT VOLTAGE AND FREQUENCY CONTROL IN THE HRES.....	20
CHAPTER 3: MAXIMUM POWER POINT TRACKING ALGORITHMS.....	22
3.1. MAXIMUM POWER POINT TRACKING ALGORITHMS.....	22
3.2. P&O METHOD.....	24
3.3. MODIFIED P&O METHOD.....	25
3.4. FUZZY LOGIC CONCEPT.....	25
CHAPTER 4: MPPT BASED ON FUZZY LOGIC CONTROL (FLC).....	27
4.1. FUZZY CONTROL FOR PV.....	27
4.2. FUZZY CONTROL FOR WIND TURBINE.....	29
CHAPTER 5: SIMULATION MODEL.....	31
5.1. SOLAR PV SIMULATION MODEL.....	31
5.2. SOLAR PV MEASUREMENT SYSTEM AND MODEL VALIDATION.....	33
5.3. PV SIMULATION MODEL VALIDATION.....	38
5.4. WIND POWER SIMULATION.....	41
5.5. SIMULATION RESULTS.....	42
CHAPTER 6: TECHNO-ECONOMIC ANALYSIS OF THE HRES.....	50
6.1. BASE CASE SCENARIO.....	53
6.2. FUTURE COST SCENARIO.....	54
CONCLUSION.....	59
REFERENCE.....	60

• Figure

Fig. 1 Energy mix in Japan (Adapted from [1]).....	7
Fig. 2 Comparison of primary energy self-sufficiency rates in major countries (2017) (Adapted from [1]).	8
Fig. 3 Japanese government's basic energy policy (Adapted from [1]).....	8
Fig. 4 Outlook for Japan's energy mix (Adapted from [1]).....	9
Fig. 5 Hybrid renewable energy system at Chikushi campus of Kyushu university.....	11
Fig. 6 Research flow.....	11
Fig. 7 PV cell mechanism ^[3]	12
Fig. 8 Equivalent circuit of a single diode PV cell.....	13
Fig. 9 Changes in the characteristic curve due to solar radiation.....	15
Fig. 10 Changes in the characteristic curve due to cell temperature.....	15
Fig. 11 Wind turbine modeling stages [5].....	16
Fig. 12 Wind turbine power coefficient vs. tip speed ratio for different pitch angles [5].....	18
Fig. 13 Structure of PMSG. Adapted from Ref. [7].....	18

Fig. 14 Buck converter.....	21
Fig. 15 Boost converter [8].....	21
Fig. 16 Incremental conductance method flow chart [3]	23
Fig. 17 PV characteristic curve ^[10]	24
Fig. 18 P&O flow chart [10]	24
Fig. 19 Crisp sets	26
Fig. 20 Fuzzy sets.....	26
Fig. 21 Structure of fuzzy controller	27
Fig. 22 Membership function for E ^[13]	28
Fig. 23 Membership function for CE ^[13]	28
Fig. 24 Power-Voltage curve of PV module.....	29
Fig. 25 Output membership function for ΔD ^[13]	29
Fig. 26 Input membership for C.....	30
Fig. 27 Input membership for CE.....	30
Fig. 28 Output membership function for ΔD	30
Fig. 29 PV Simulink model.....	31
Fig. 30 Fuzzy controller Simulink model	31
Fig. 31 Schematic diagram of the buck converter.....	32
Fig. 32 (1) Wind turbine, (2) Weather measurement station, (3) Datalogger, (4) Inverter, (5) PV DC converter and controller,(6) Wind DC converter and controller, (7) Pyranometer, (8) PV module, (9) Battery [5]	33
Fig. 33 Pyranometer.....	35
Fig. 34 Measured data on solar radiation.....	36
Fig. 35 Cell temperature measurement system	37
Fig. 36 Comparison of measured and calculated cell temperature	37
Fig. 37 PV power measurement device.....	38
Fig. 38 I-V curve of the 50W solar panel (Measured at 12:40 on September 23, 2020).....	39
Fig. 39 P-V curve of the 50W solar panel (Measured at 12:40 on September 23, 2020).....	39
Fig. 40 I-V curve of the 160W solar panel (Measured at 12:45 on September 23, 2020).....	40
Fig. 41 P-V curve of the 160W solar panel (Measured at 12:45 on September 23, 2020).....	40
Fig. 42 Wind generator Simulink model.....	41
Fig. 43 Simulink model of the fuzzy controller for wind generator.....	42
Fig. 44 Solar irradiance and cell temperature at 10am on April 14 in 2020.....	43
Fig. 45 PV power of the fuzzy and P&O on April 14 in 2020.....	43
Fig. 46 Solar irradiance and cell temperature at 10am on July 17 in 2020	44
Fig. 47 PV power of the fuzzy and P&O on July 17 in 2020	44
Fig. 48 Solar irradiance and cell temperature at 10am on October 22 in 2020.....	45
Fig. 49 PV power of the fuzzy and P&O on October 22 in 2020.....	46
Fig. 50 Wind speed on April 1, 2020.....	48
Fig. 51 Power generated by wind turbine.....	48
Fig. 52 Wind speed on April 2, 2020.....	49
Fig. 53 Power generated by wind turbine.....	49
Fig. 54 HOMER simulation model.....	51
Fig. 55 Hourly power consumption in each month.....	51
Fig. 56 Trends in initial capital cost of PV (Adapted from [22]).....	55
Fig. 57 Initial capital cost of Wind turbine (Adapted from [23]).....	55
Fig. 58 Electricity supply and COE for HRES and grid in each model.....	57
Fig. 59 Power generation of the PV system in each model.....	57
Fig. 60 Power generation of the Fuel cell in each model.....	58

• Table

Table. 1 Fuzzy rule for PV	28
Table. 2 Fuzzy rule for WECS	30
Table. 3 Specs of the solar panel	32
Table. 4 Parameter of the buck converter	32
Table. 5 Battery parameters	33
Table. 6 Battery charge controller parameters	34
Table. 7 Pyranometer specification [14]	35
Table. 8 160W and 50W PV panel spec.....	39
Table. 9 Measurement and simulation results for 50W solar panel.....	40
Table. 10 Measurement and simulation results for 160W solar panel.....	41
Table. 11 Wind generator parameters	41
Table. 12 Parameter of the buck converter.....	42
Table. 13 1day simulation results on April 14	43
Table. 14 1day simulation results on July 17.....	45
Table. 15 1day simulation results on October 22	46
Table. 16 Date the simulation was performed.....	47
Table. 17 1year simulation results.....	47
Table. 18 Specification of PV system [18].....	52
Table. 19 Costs of components and economic data.....	53
Table. 20 Component capacity and electricity production	53
Table. 21 Cost Analysis Comparison of P&O and Fuzzy Controller	54
Table. 22 Summary of current and future initial capital costs.....	55
Table. 23 Summary of COE for each model.....	56
Table. 24 Size of each component of the HRES.....	56
Table. 25 Power generation from each component of the HRES.....	57

Abstract

Thermal power generation accounts for the majority of power generation in Japan. In particular, after the Great East Japan Earthquake, the dependence on thermal power generation has increased rapidly due to growing concerns about nuclear power. In order to tackle environmental issues such as global warming, cleaner power generation systems should be used. Furthermore, Japan's energy self-sufficiency rate is relatively low compared to other developed countries. Thus, Japan's power sector needs to be improved from both environmental and energy security perspectives. Renewable energy is an effective countermeasure to increase resilience and reduce emissions. However, since renewable energy comes from the natural environment, it is dependent on the climate; therefore, it is unstable. The hybridization of variable renewables can allow for smooth, durable, and reliable output to power grids to improve the safety, reliability, and stability of dispatched power, which is cheaper than investing in single renewable technologies.

In order to reduce the load demand of buildings in Japan, this study proposes a grid-tied hybrid solar-wind system, which is envisioned to be installed at Kyushu University's Chikushi Campus in Kasuga, Japan. The proposed system consists of three PV modules with a total power of (480W), a wind turbine (400 W), and an Inverter (1000 W), which was installed on the rooftop of Building E, in Chikushi Campus. The proposed HRES is equipped with an advanced Fuzzy Logic Control (FCL), which provides rapid control, and small oscillations once the Maximum Power Point (MPP) is tracked and shows good performance under varying weather conditions. The dynamic modeling and simulation of the proposed HRES system were performed in MATLAB -Simulink.

The techno-economic analysis of the proposed system was performed in HOMER software, aiming to estimate the optimal configuration of the proposed HRES subject to satisfying the required annual load in the Chikushi campus. Furthermore, it addresses how the Levelized Cost of Energy (COE) for the FLC-based system is lower than the conventional Perturb and Observes (P&O)-based systems. A sensitivity analysis is also carried out to assess the feasibility of the proposed HRES, using the future market price of renewable energy technologies in 2030. To this aim, two different scenarios were introduced in this study. The base scenario was defined based on the current market cost of renewable energy systems. The impact of the future costs of each component (Solar, Wind, Fuel Cell) of HRES in 2030 was evaluated in three scenarios: Scen (1): future costs were only applied to PV systems, Scen (2): future costs were only applied to hydrogen systems, and Scen (3): future costs were applied to all components. There is a significant difference in the COE between Scenarios (1) and (2). This is because the only energy source for the electrolyzer that supplies hydrogen to the fuel cell is the PV system's electricity. The future decline in the solar system's market cost, which is the largest energy source in the HRES, is essential for improving the COE. This study proves that larger systems can be installed if the costs of installing and maintaining renewable energy systems are reduced as expected.

Acknowledgment

First of all, I would like to express my gratitude to Associate Professor Hooman Farzaneh to support my master's research. I am thankful to Ayas Shaqour, who shared with me some ideas and assistance. I am thankful to all of the members of our laboratory members (Energy and Environment System Lab.) and staff for their help and cooperation. I am also grateful to all of my teachers and colleagues for their kind support and inspiration during this research.

Tatsuya Hinokuma

Chapter 1: Introduction

1.1. Energy situation in japan

Today, the earth faces a big environmental problem, which is global warming. Renewable energy is one of the best ways to solve this problem. After the Great East Japan Earthquake, the proportion of nuclear power generation in Japan has decreased significantly. This is because the public's concern about nuclear power plants has increased due to the nuclear accident. As a result, the dependence on thermal power generation has increased. As a result, the reliance on thermal power has increased, as shown in Fig.1 [1]. However, Japan lacks energy resources, and as shown in Fig.2, its energy self-sufficiency rate is meager compared to other OECD countries. [1]. This is a severe problem from the perspective of energy security. It is also necessary to reduce this dependence on fossil fuels in order to stop global warming that has been called for in recent years. Renewable energy will play an essential role in solving these problems.

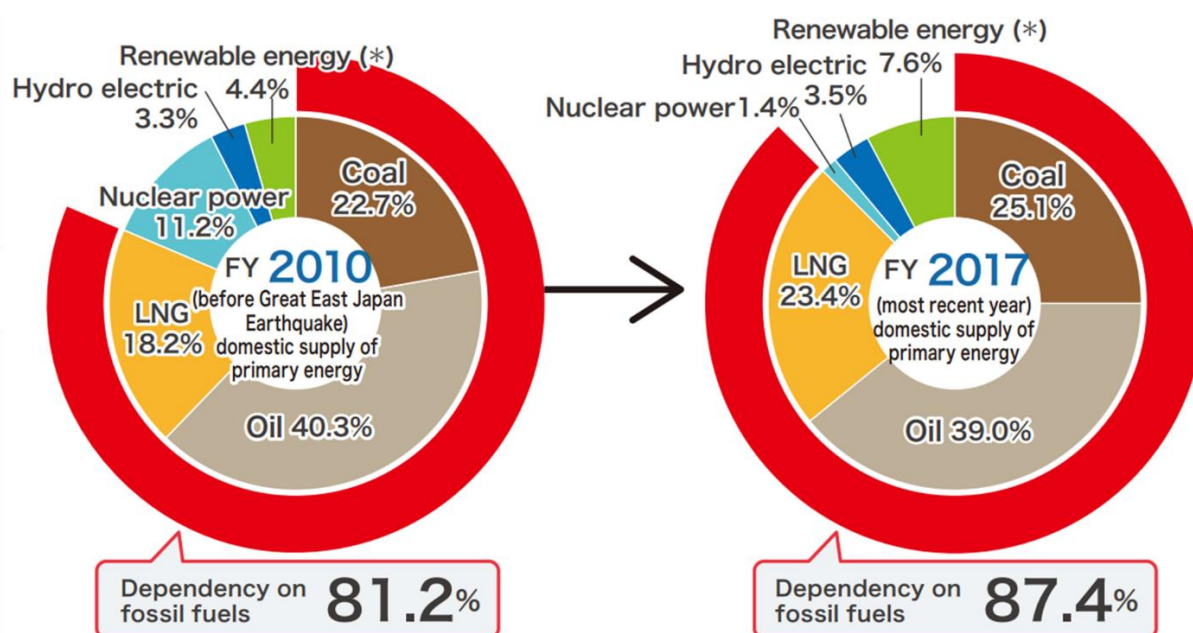


Fig. 1 Energy mix in Japan (Adapted from [1])

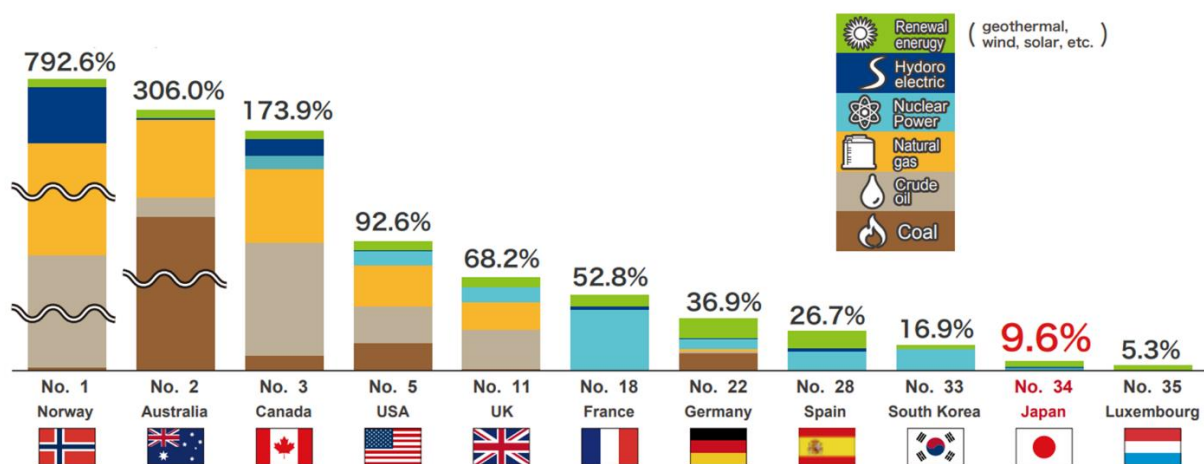


Fig. 2 Comparison of primary energy self-sufficiency rates in major countries (2017) (Adapted from [1])

1.2. Future plans of the renewable energy system in Japan

The Japanese government promotes an initiative (3E+S) to achieve energy security, economic efficiency, and environmental compatibility, with safety as the priority. A schematic diagram of this initiative is shown in Figure 3. In order to cope with the shortage of resources in Japan, it is necessary to realize a hybrid energy supply systems that maximize the use of each energy source and compensate for its weaknesses. Figure 4 shows the energy mix that can be achieved in 2030, if measures are taken according to the Japanese government's policies.

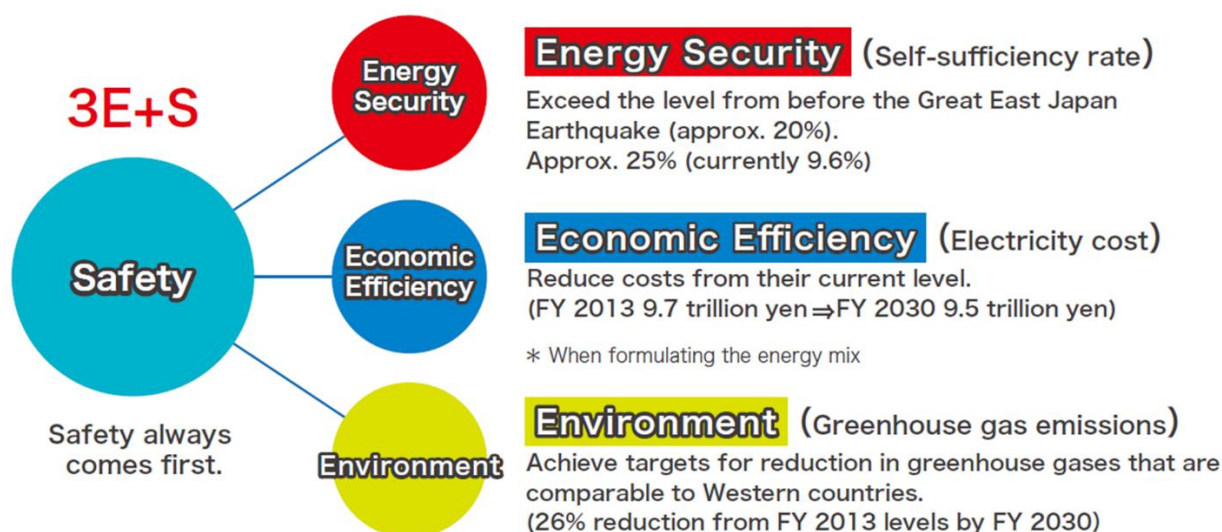


Fig. 3 Japanese government's basic energy policy (Adapted from [1])

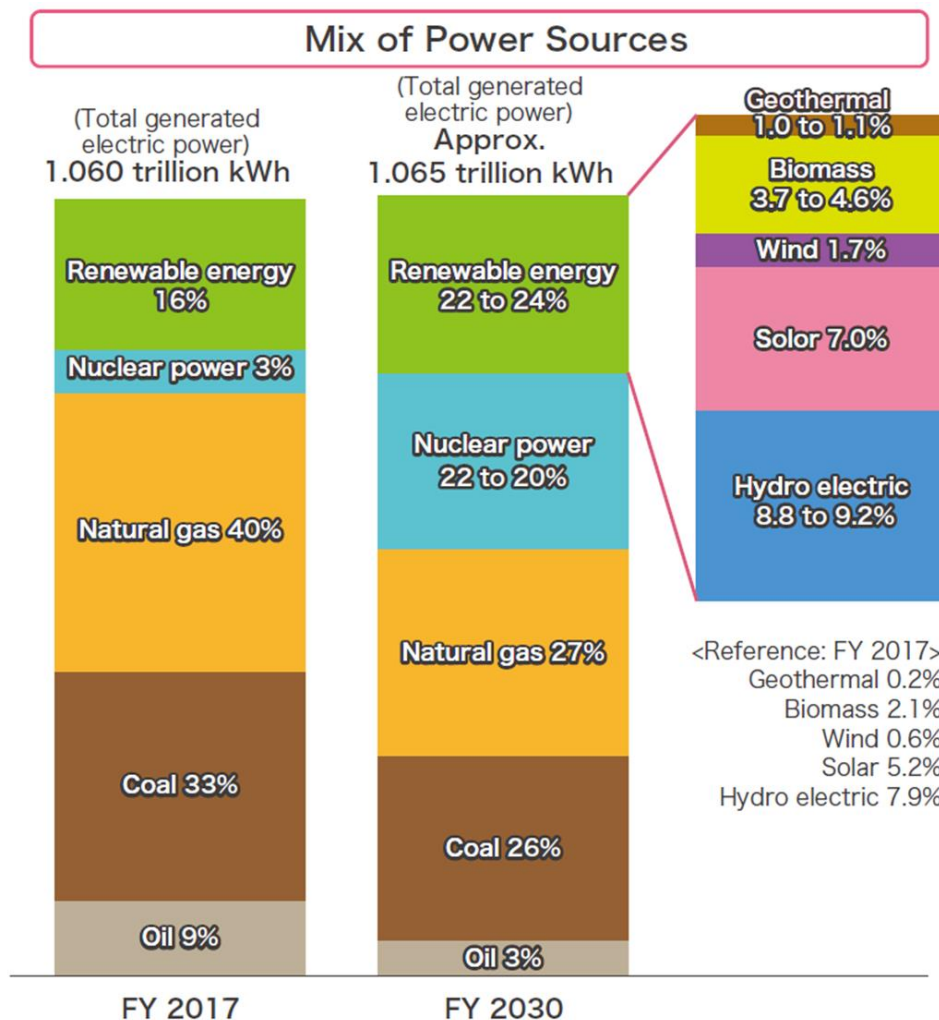


Fig. 4 Outlook for Japan's energy mix (Adapted from [1])

1.3. Hybrid Renewable Energy System

As mentioned above, renewable energy effectively addresses environmental issues, and Japan's resource shortage. However, because they use energy from nature, they have the weakness of being subject to climate change and unstable. For example, solar power alone cannot provide enough energy on rainy days. Hybridization of multiple renewable energy systems can be considered as a solution to overcome this weakness. Hybrid Renewable Energy Systems (HRES) can utilize different renewable energy sources and operate flexibly in variable climatic conditions to achieve a stable power supply. When the various renewable energy sources are integrated as a single hybrid system, the advantages of one source compensate for the disadvantages of the others. As a result, better efficiency can be obtained, and overall cost reduction can be expected. [2]

1.4. What will be elucidated in this research

This study aims to introduce a novel Hybrid Renewable Energy System (HRES) equipped with an advanced Maximum Power Tracking (MPPT) system shown in Fig.5. The overall research flow diagram is depicted in Fig.6. The first part of this study focuses on the detailed dynamic simulation of the technical performance of the proposed HRES. The output power of the proposed HRES varies on environmental variables such as solar irradiance, wind, and operating temperature. The MPPT control technique is mainly used to extract the maximum capable power of the HRES with respective solar irradiance, wind speed, and temperature at a particular instant of time point. Many algorithms have been developed to efficiently track the maximum power point, such as Incremental Conductance (INC), Hill Climbing, or Perturbation and Observation (P&O)¹. There are two concerns with the existing MPPT algorithms: 1) Most of them suffer from the drawback of being slow tracking, due to which the utilization efficiency is reduced; 2) Furthermore, intermittency and rapid irradiation and temperature changes may cause the MPPT to be oscillating around one of the multiple local peaks of power.

To overcome the drawbacks mentioned above, this study will introduce a novel MPPT system based on FLC, which provides rapid control, and small oscillations once it reached the MPP and good performance under varying weather conditions. A detailed dynamic simulation will be performed in MATLAB Simulink to simulate the technical performance of the PV arrays and wind turbine, and then a Maximum Power Point tracking method using Fuzzy Logic Control (FLC) system is proposed in order to control the DC-DC converter. The proposed HRES is envisioned to be installed at Kyushu University's Chikushi Campus in Kasuga, Japan. The experimental setup was installed on the rooftop of the Energy and the Environmental Systems (EES) laboratory at Chikushi campus, Kyushu University, Japan. The test pilot consists of three PV modules with a total power of (480 W), a wind turbine (400 W), a lead-acid battery (30 Ah), and an inverter. Furthermore, the simulation model will be tested, using the real measured data on incident solar radiation on the PV panels and cell temperature in the local field. The detailed meteorological data used in this study are collected from the Japan Meteorological Agency for Fukuoka City.

The second part of the study discusses a detailed Techno-Economic Analysis (TEA) of the proposed HRES, including the hydrogen production and storage components. TEA is used to find the optimal configuration of the HRES and to verify the balance of electricity and hydrogen generation for securing the operation feasibly during the system lifetime.

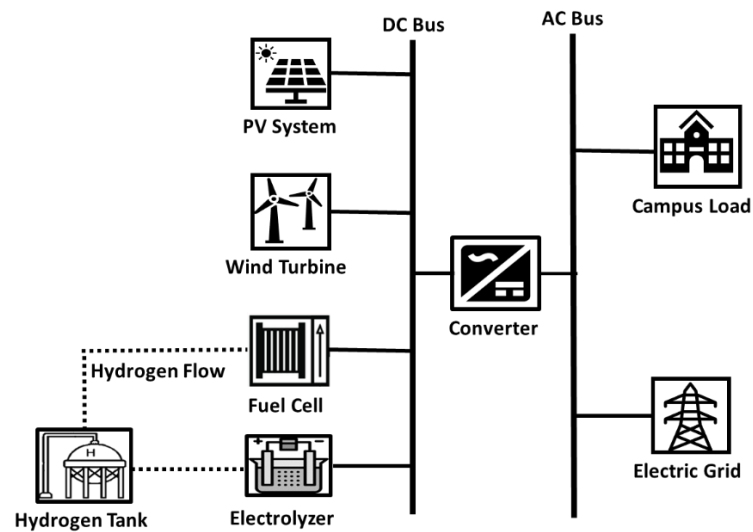


Fig. 5 Hybrid renewable energy system at Chikushi campus of Kyushu university

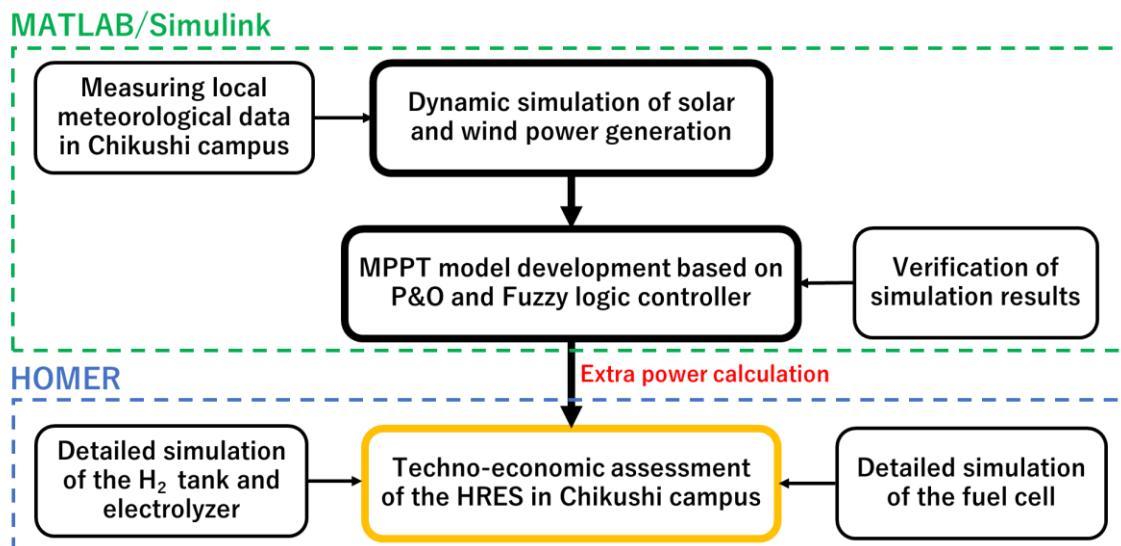


Fig. 6 Research flow

In this thesis, chapters 2 and 3 describe the basic power generation mechanisms and power simulation methods for PV and wind power. Chapters 4 and 5 discuss currently proposed methods of maximum power tracking control. Chapter 6 describes the FLC and its application to PV systems and wind turbines. Chapter 7 describes the simulation results of the fuzzy controller and P&O controller based on the local climatic conditions. The fuzzy controller shows better-tracking performance and speed than the P&O. In Chapter 8, the simulation of HOMER Pro is described. Here, the fuzzy controller proves to be superior to the P&O. Furthermore; the future cost-based scenario confirms the potential of renewable energy itself in reducing the cost of the system.

The most significant results obtained in this study are the fuzzy controller's effectiveness and the economic benefits derived from it.

Chapter 2: Fundamental of the solar and wind power generation

2.1. Principle of power generation by the solar cell

The solar cell is composed of p-type silicon and n-type silicon, as shown in Fig.7. Charge carriers can only move in one direction, from the p region to the n junction. There are three steps to generate electricity. First, solar radiation reaches the boundary of p-type and n-type semiconductors. It then being excited by radiation, electrons move to the n-type semiconductor. Finally, an n-type semiconductor becomes a negative electrode, and p-type silicon becomes a positive electrode. Thus, when receiving the solar radiation, the solar cell can generate electricity.

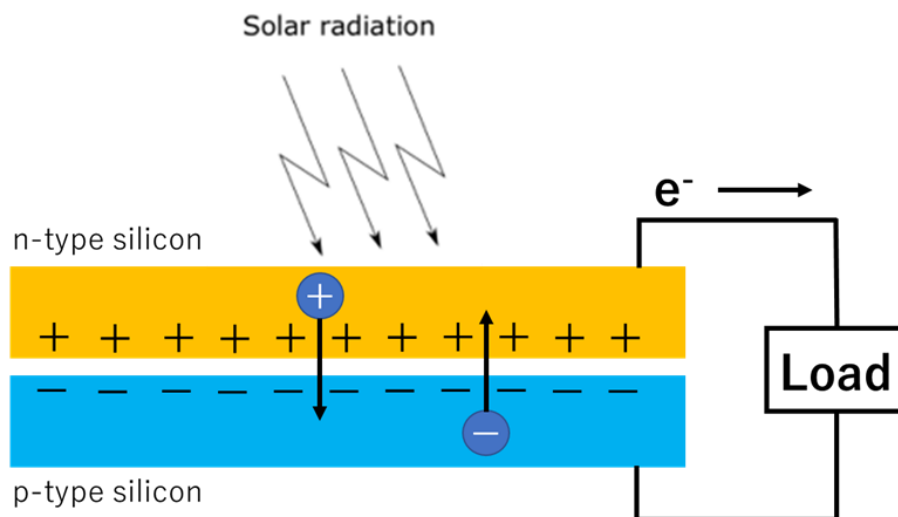


Fig. 7 PV cell mechanism ^[3]

2.1.1. Equivalent electric circuit of a solar cell

A PV panel is composed of several cells, and each cell has its electric circuit. There are two types of cell circuits: the single diode model and the two-diode model. In this research, the single diode model is used. Fig.8 represents the equivalent circuit of the single diode model.

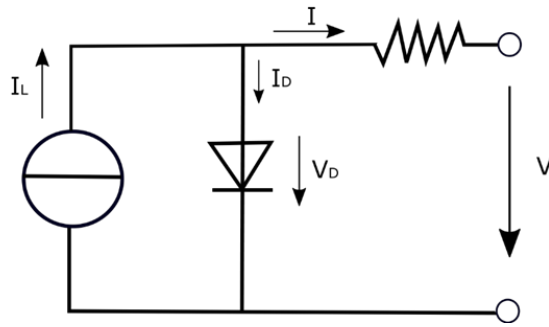


Fig. 8 Equivalent circuit of a single diode PV cell

As can be observed from Fig.2, I_L and I_D express the light current and the diode current. The total output current from a cell can be calculated as follows:

$$I = I_L - I_D \quad (1)$$

The light current I_L is expressed by the following formula [4].

$$I_L = \frac{G}{G_{STC}} \times [I_{L,STC} + k_t(T_{cell} - T_{cell,STC})] \quad (2)$$

Where:

G : solar irradiance on the PV surface [kW/m^2]

G_{STC} : solar irradiance on PV surface at STC [kW/m^2]

$I_{sc,STC}$: short circuit current at STC [A]

k_t : coefficient of I_{sc} [$\text{mA}/^\circ\text{C}$] = 1.81 [$\text{mA}/^\circ\text{C}$]

$T_{cell,STC}$: cell temperature at STC [K]=298[K]

The diode current is calculated as follows [4].

$$I_D = I_0 \left[\exp \left(\frac{q \times (V + IR_s)}{k \times T_{cell} \times nI \times N_{cell}} \right) - 1 \right] \quad (3)$$

Where:

I_{sc} : short circuit current [A]=6.03[A]

I_0 : diode saturation current [A]

V : diode voltage [V]

k : Boltzman constant = 1.3806e-23 [J/K]

T_{cell} : cell temperature [K]

q : electron charge = 1.6022e-19 [C]

nI : diode ideality factor, a number close to 1.0

N_{cell} : number of cells connected in series in a module

I : the output current from a solar cell

R_s : the series resistance

But in the real situation, Eq (3) is too complicated to calculate the diode current. So, in this research, it is assumed that the series resistance is 0. Therefore:

$$I_D = I_0 \left[\exp \left(\frac{q \times V}{k \times T_{cell} \times nI \times Ncell} \right) - 1 \right] \quad (4)$$

The diode saturation current I_0 can be written as:[4].

$$I_0 = I_{0,STC} \left(\frac{T_{cell}}{T_{cell,STC}} \right)^3 \exp \left[\left(\frac{q\varepsilon_G}{k} \right) \left(\frac{1}{T_{cell,STC}} - \frac{1}{T_{cell}} \right) \right] \quad (5)$$

ε_G is the material bandgap energy [eV]=1.12[eV]

Furthermore, $I_{0,STC}$ is given by the following equation [4].

$$I_{0,STC} = \frac{I_{sc,STC}}{\left[\exp \left(\frac{V_{oc} \times q}{k \times T_{cell} \times nI \times Ncell} \right) - 1 \right]} \quad (6)$$

Finally, Eq (1) can be replaced by Eq (7) as follows:[4].

$$I = \frac{G}{G_{STC}} \times [I_{L,STC} + k_t(T_{cell} - T_{cell,STC})] + I_0 \left[\exp \left(\frac{q \times V}{k \times T_{cell} \times nI \times Ncell} \right) - 1 \right] \quad (7)$$

2.1.2. PV characteristic curve

There is a maximum power point in the form of a power characteristic curve of the PV array, and its position changes under the influence of climatic conditions. In order to find this point, maximum power point tracking control is necessary. Figure 9 shows the I-V curve and P-V curve when the solar radiation changes from 0.5kW/m², 0.8kW/m² to 1kW/m². As solar irradiation increases, MPP shows a higher value. If a part of the PV panel is shaded, its power generation capacity will be significantly reduced even if 1 kW/m² of solar radiation is falling on the unshaded area.

Furthermore, the power generation of a PV panel is also greatly affected by the cell temperature. Figure 10 shows the I-V and P-V curves of a PV panel when the cell temperature is 0°C, 25°C, and 50°C. As the temperature increases, the efficiency of the PV panel decreases, and the amount of electricity obtained decreases. Thus, MPPT is a function to track the MPP, which continually varies with solar radiation and temperature changes.

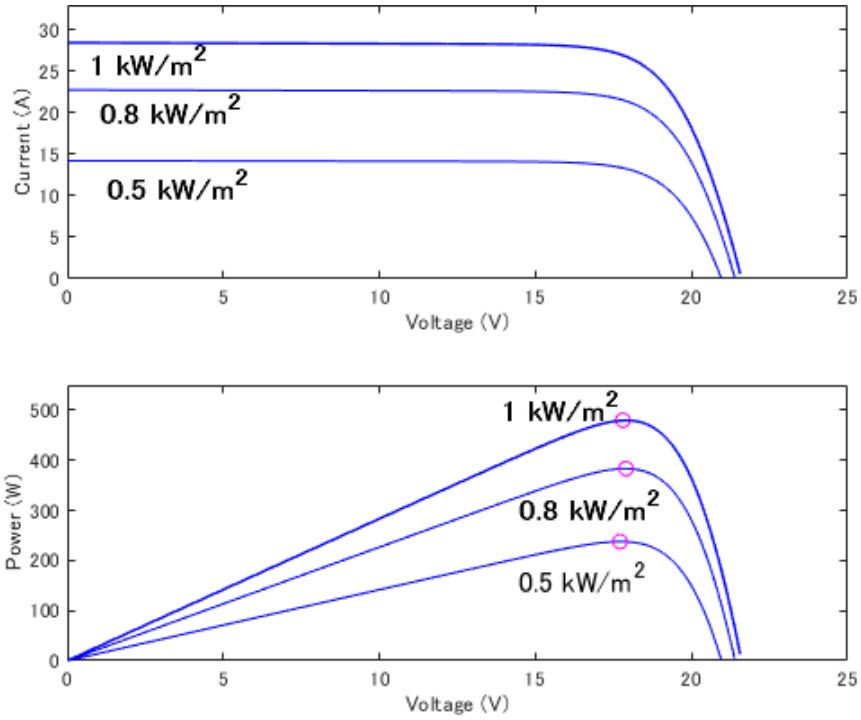


Fig. 9 Changes in the characteristic curve due to solar radiation

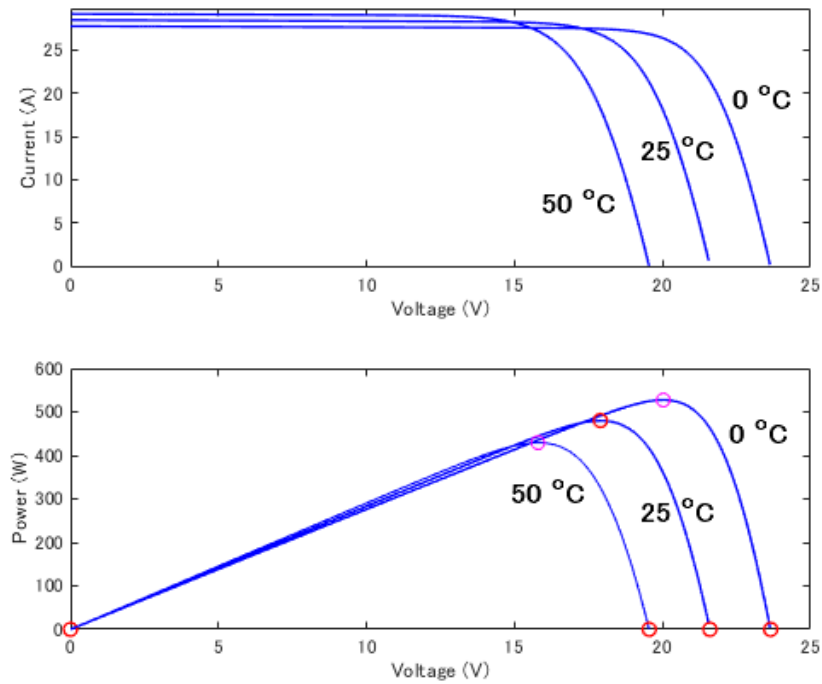


Fig. 10 Changes in the characteristic curve due to cell temperature

2.2. Fundamental of the wind power generator

A wind power generator system is composed of three stages, as shown in Fig.17 [6]. In the aerodynamics stage, kinetic energy in the air is converted to mechanical rotational energy. Next, in the mechanical stage, the wind turbine is controlled by the gearbox to adjust the torque-speed that will be an input to the generator. The generator transforms mechanical energy into an electrical 3-phase signal. Finally, the 3-phase electrical signal is controlled and transformed into different voltage levels, using converters and inverters.

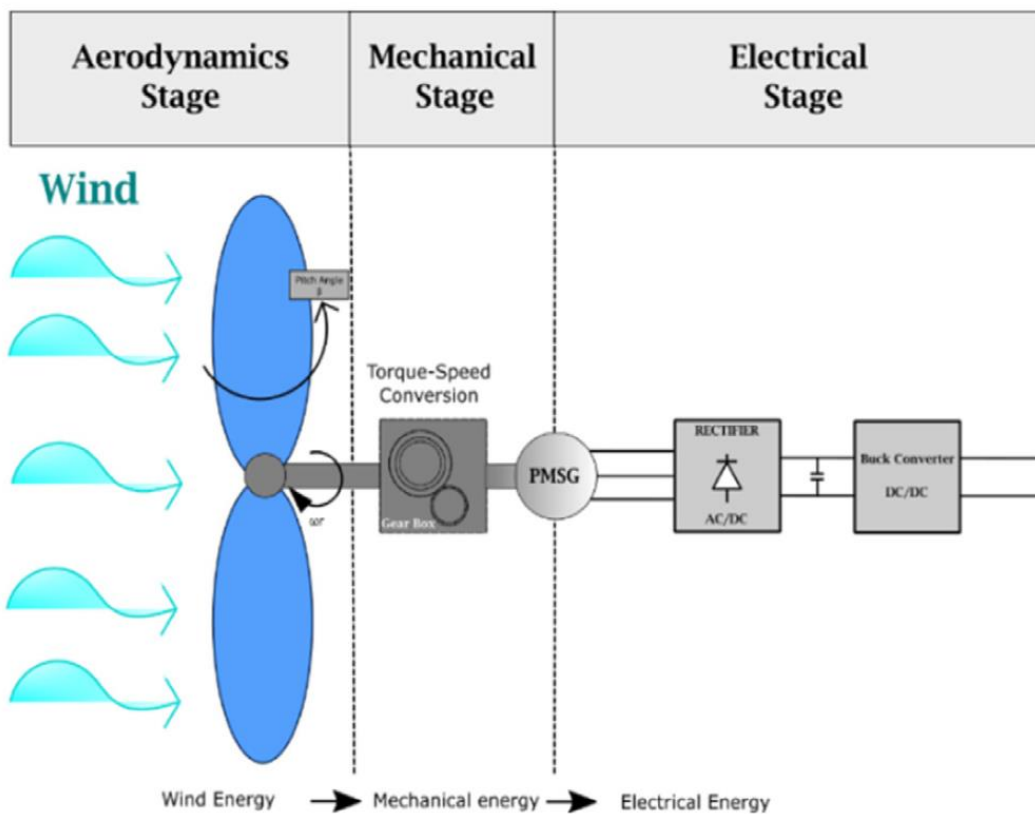


Fig. 11 Wind turbine modeling stages [5]

The wind stream power is expressed by equation (8).

$$P_{air} = \frac{1}{2} \rho A V_w^3 \quad (8)$$

Where:

P_{air} : power from the wind

ρ : air density [kg/m³]

A : cross-sectional area [m²]

V_w : wind velocity [m/s]

The mechanical power generated by the wind turbine can be calculated by equation (9) [6].

$$P_m = \frac{1}{2} C_p(\lambda, \beta) \rho A V_w^3 \quad (9)$$

Where:

P_m : mechanical power generated by wind turbine

C_p : wind turbine power coefficient

λ : tip speed ratio

β : pitch angle[°]

The power coefficient C_p indicates the power extraction efficiency of the wind turbine. This coefficient is estimated, using the tip speed ratio λ and the pitch angle β , as shown in equation (10) [5]. C_p is a nonlinear function of the tip speed ratio and the blade pitch angle.

$$C_p = 0.5176 \left(\frac{116}{\lambda_i} - 0.4\beta - 5 \right) e^{\frac{-21}{\lambda_i}} + 0.0068\lambda \quad (10)$$

And λ_i is calculated by equation (11) and (12).

$$\frac{1}{\lambda_i} = \frac{1}{\lambda + 0.08\beta} - \frac{0.035}{\beta^3 + 1} \quad (11)$$

$$\lambda = \frac{\omega_{wt} R}{V_w} \quad (12)$$

Where:

ω_{wt} : rotational speed of the wind turbine [rad/s]

R : turbine blade radius [m]

C_p becomes the maximum value 0.48 when β is 0° and λ is 8.1. And this value of λ is called the nominal tip speed ratio.

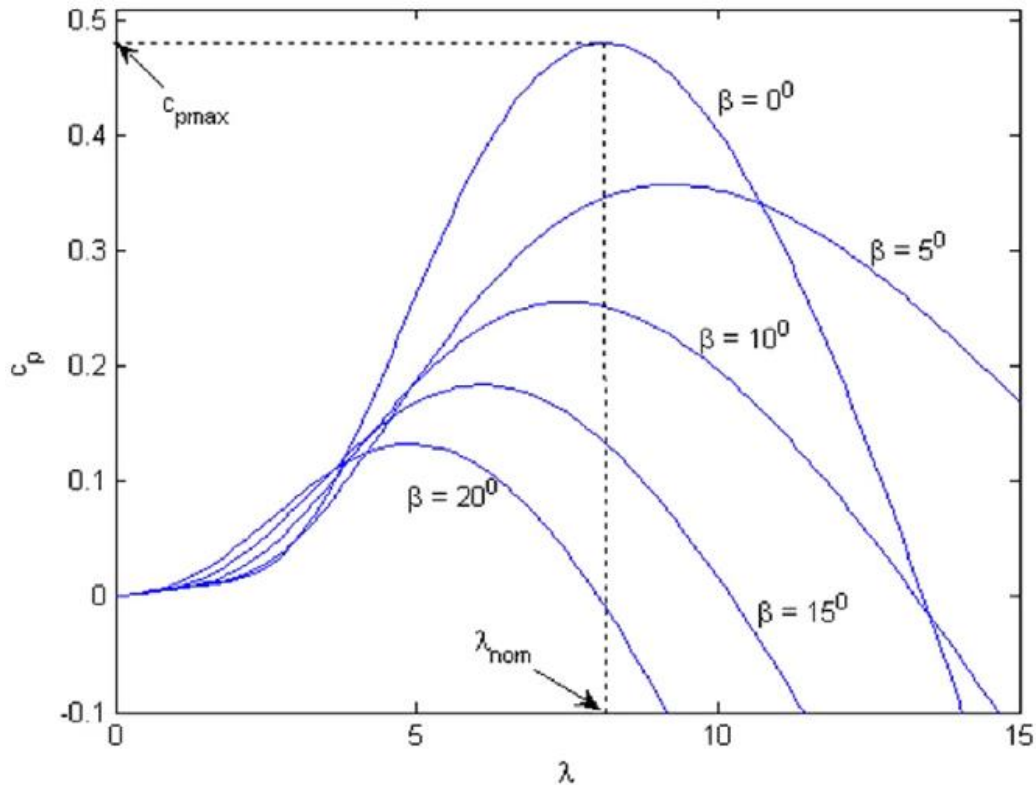


Fig. 12 Wind turbine power coefficient vs. tip speed ratio for different pitch angles [5]

2.2.1. Permanent Magnet Synchronous Generator (PMSG)

Figure 19 shows a PMSG, with a rotor in the center and three coils surrounding it. The magnetic flux of the three coils is synthesized in the rotor region and becomes the rotational speed. This rotational magnetic flux generation causes the permanent magnet at the center to start rotating, completing the synchronous generator. The PMSG has a permanent magnet instead of an electromagnet in the rotor, so there is no need to supply the magnetic field current from outside. Therefore, there is no power feeding structure, and the system is simple.

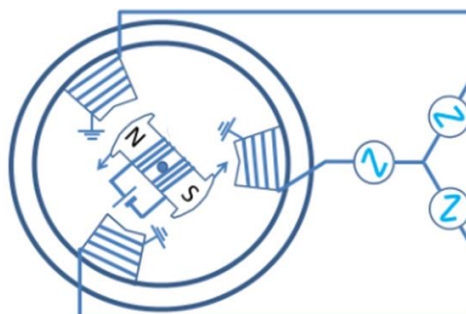


Fig. 13 Structure of PMSG. Adapted from Ref. [7]

The voltage and current of PMSG are calculated by the following equations [5]. d and q refer to the direct-axis and quadrature-axis components, respectively. The active and reactive electrical powers of the stator are calculated by equation (16).

$$\frac{d}{dt}i_d = \frac{1}{L_d}v_d - \frac{R}{L_d}i_d + \frac{L_q}{L_d}pi_q\omega_m \quad (13)$$

$$\frac{d}{dt}i_q = \frac{1}{L_q}v_q - \frac{R}{L_q}i_q + \frac{L_d}{L_q}pi_d\omega_m - \frac{\lambda p\omega_m}{L_q} \quad (14)$$

$$L_d = L_q = \frac{L_{ab}}{2} \quad (15)$$

$$P_s = v_d i_d + v_q i_q, \quad Q_s = v_d i_q + v_q i_d \quad (16)$$

Where:

ω_m : angular velocity of the rotor

λ : magnitude of the flux caused by the permanent magnet of the rotor

p : number of pole pairs

v : voltage

i : current

R : resistance of the stator

L_d : direct-axis inductance

L_q : quadrature-axis inductance

L_{ab} : the inductance from phase to phase

The electrical torque T_e is derived as equation (17).

$$T_e = \frac{3}{2}p[\lambda i_q + (L_d - L_q)i_d i_q] \quad (17)$$

And the relation of the torque and rotor angular velocity is calculated by the following equation (18).

$$\frac{d}{dt}\omega_m = \frac{1}{J}(T_e - T_f - F\omega_m - T_m), \quad \frac{d\theta}{dt} = \omega_m \quad (18)$$

J : inertia of the rotor and load

F : viscous friction of the rotor and load

θ : angular position

T_m : shaft mechanical torque

T_f : shaft static friction torque

2.2.2. Rectifier

A three-phase uncontrolled diode rectifier is introduced to convert the three-phase AC output obtained from the PMSG to DC. The rectifier's output voltage can be calculated by the following equation [8].

$$v_0(t) = V_0 + \sum_{n=6,12,18\dots}^{\infty} V_n \cos(n\omega_0 t + \pi) \quad (19)$$

And dc voltage V_0 and the amplitudes of the voltage terms are calculated by the following equations. $V_{m,L-L}$ is the line-to-line peak voltage of the wind turbine generator output and is equal to $\sqrt{2}V_{L-L,rms}$. The harmonics found in equation (20) are of order $6k+1$ ($k = 1, 2, 3, \dots$), which allows us to remove the low amplitude high-frequency components [5].

$$V_0 = \frac{3V_{m,L-L}}{\pi} = 0.955V_{m,L-L} \quad (20)$$

$$V_n = \frac{6V_{m,L-L}}{\pi(n^2 - 1)} \quad (21)$$

2.3. Output voltage and frequency control in the HRES

A DC-DC converter is needed to control the power of renewable energy. This DC-DC converter controls the renewable energy system's output voltage by adjusting the duty ratio, allowing it to find the maximum power point. Two typical forms of dc-dc converters are introduced below.

Buck converter

Figure 14 shows the circuit diagram of the buck converter, which consists of a switch, a diode, an inductor, and a capacitor. The buck converter is responsible for hardening the voltage [5]. By repeatedly switching the circuit on and off at high frequencies, the buck converter can control and drop the output voltage to the required level. When the switch is ON, the current flows from the input power supply to the inductor, converting electrical energy into magnetic energy and storing the energy in the inductor. Then, when the switch is turned off, the magnetic energy stored in the inductor is supplied to the load on the output side as electrical energy again. This ON/OFF is adjusted to output a constant voltage to the output side.

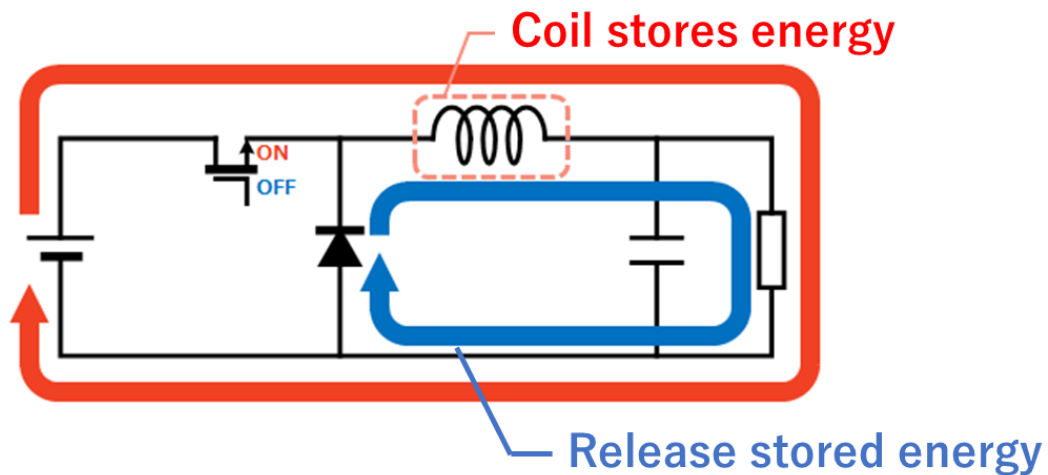


Fig. 14 Buck converter

Boost converter

Figure 15 shows the circuit diagram of the boost converter. In this boost converter, the components used are the same, and the voltage conversion is done by the inductor storing energy and adjusting ON/OFF. However, the circuit structure is different from that of the buck converter. Compared to the buck converter, the inductor, switch, and diode are in different positions. When the switch is ON, energy is stored in the inductor. On the other hand, when the switch is off, the input power supply and the energy stored in the inductor are combined and supplied to the output side. As a result, an output voltage higher than the input voltage can be achieved.

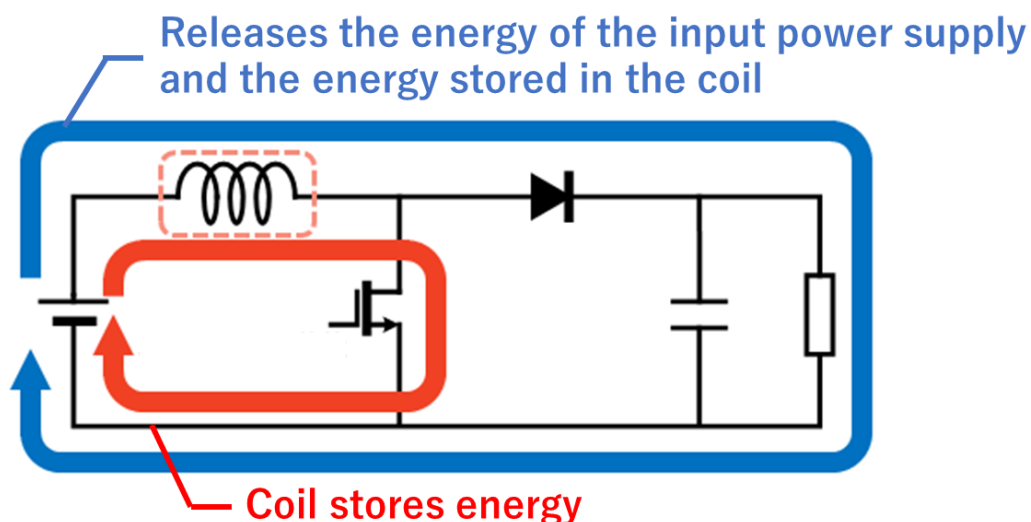


Fig. 15 Boost converter [8]

Chapter 3: Maximum Power Point Tracking algorithms

3.1. Maximum Power Point Tracking algorithms

Maximum power point tracking (MPPT) is the method to extract the maximum power from renewable energy. For example, when a PV module generates electricity by receiving solar radiation, the operating point (OP) is always affected by weather conditions (solar radiation, ambient temperature) and shifts. To achieve maximum power, it is necessary to adjust the load and output a proper voltage. The MPPT algorithm can change the OP of the PV module by adjusting the duty cycle of the DC-DC converter. Thus, the MPPT algorithm is an important concept for renewable energy to output the maximum power. There are many MPPT techniques. The following part says about explanations of some MPPT techniques which are commonly used, except P&O and the fuzzy logic technique.

Constant voltage technique

The constant voltage technique is one of the simplest MPPT methods. This technique fixes the voltage at a specific value. Therefore, in this method, the OP never corresponds to MPP. And it is essential to decide the fixed voltage value by considering a PV module's technical specifications and weather conditions. This technique works well at low-level solar radiation, and so it is often combined with other MPPT techniques [9].

Open voltage technique

The open-circuit voltage method assumes that the open-circuit voltage (V_{oc}) is approximated to the voltage at the maximum power point (V_{mpp}) [3]. This approximation is made by Equation 22. where K_v is a proportionality constant. This K_v will vary depending on the performance of the solar panel and the natural environment of the area where it is installed. Therefore, it is necessary to investigate V_{oc} and V_{mpp} at different temperatures and solar radiation levels beforehand. This method has a simple structure and does not require a controller, thus lowering its cost. Besides, it is possible to operate the system even under low solar radiation. On the other hand, it has the disadvantage that it is difficult to obtain the same maximum power because it uses an approximate formula.

$$V_{mpp} \sim k_v \times V_{oc} \quad (22)$$

Incremental conductance technique

This incremental conductance (INC) method compares the conductance of the PV system with its derivative (dI_{pv}/dV_{pv}) in order to estimate the location of the operating points [3]. The position of each operating point found by this comparison is shown in the following equations [3]. The operation analyzed by this method is shown in Fig. 16 as a flowchart.

This method is considered to be logically superior to the P&O method. However, it is difficult to find the true MPP due to oscillations and losses caused by noise and measurement errors in practice. It also requires more time to track due to its complex calculations. In order to reduce these problems, measures

such as increasing the sampling time step (t) have been taken.

$$\frac{dI_{pv}}{dV_{pv}} = -\frac{I_{pv}}{V_{pv}} \quad \text{at the MPP} \quad (23)$$

$$\frac{dI_{pv}}{dV_{pv}} > -\frac{I_{pv}}{V_{pv}} \quad \text{at the left side of the MPP} \quad (24)$$

$$\frac{dI_{pv}}{dV_{pv}} < -\frac{I_{pv}}{V_{pv}} \quad \text{at the right side of the MPP} \quad (25)$$

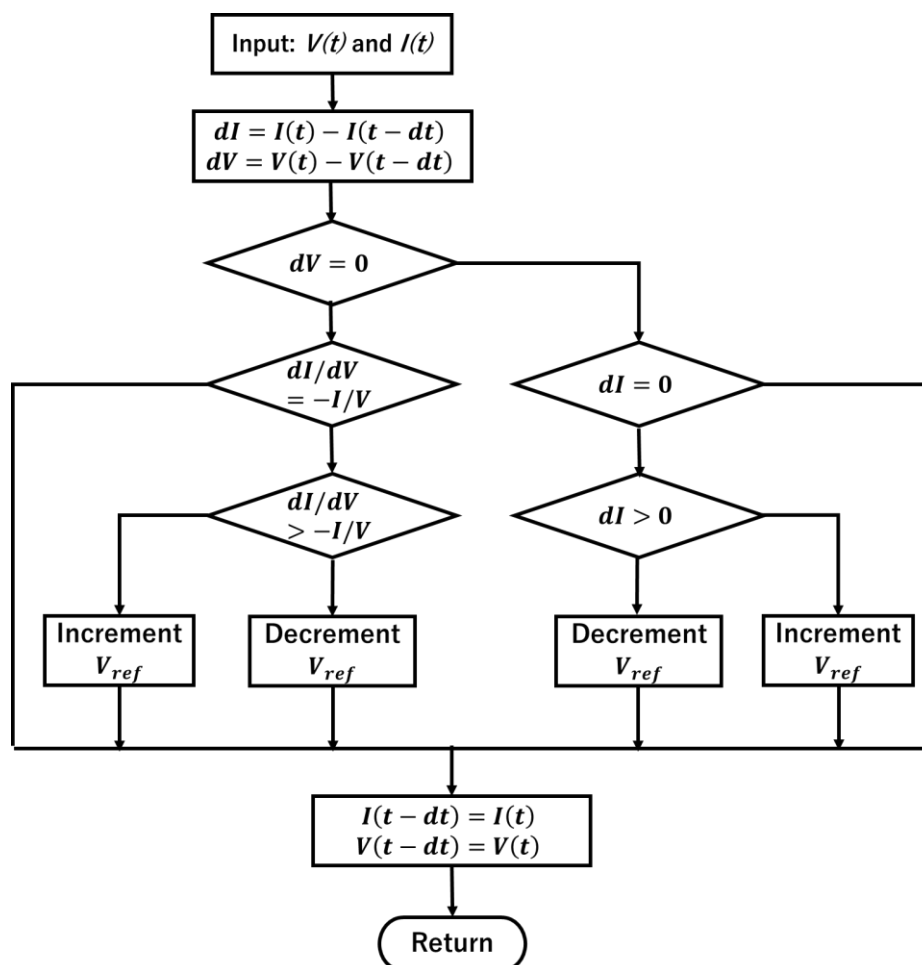


Fig. 16 Incremental conductance method flow chart [3]

3.2. P&O method

The Perturb and Observe (P&O) controller increases or decreases the duty cycle to bring the operating point (OP) close to the MPPT on the PV curve, as shown in Fig.1. The step size of ΔD is fixed. For example, the OP is on the left side of the MPP; the P&O controller decreases the duty cycle to increase the voltage. When the OP is on the MPP's right side, the P&O controller increases the duty cycle to reduce the voltage. Figure 2 shows the detailed P&O algorithm. This is a very general method to control the voltage of the PV panel, since it is simple and low cost.

On the other hand, P&O has some demerits. The convergence speed is slow, and the result has a lot of fluctuation. These defects are caused by fixed ΔD . If being significantly on the left side of the MPP, the PO gradually gets closer to the MPP at the same step size. At the MPP, the OP passes by the MPP because of the same step size. This point oscillates around the MPP. These are reasons for P&O demerits. If the step size is very small to reduce oscillations around the MPP, the OP takes more time to reach the MPP. Conversely, if the step size is large to shorten the time to reach the MPP, the result has many fluctuations around the MPP. These are the reason for P&O demerits.

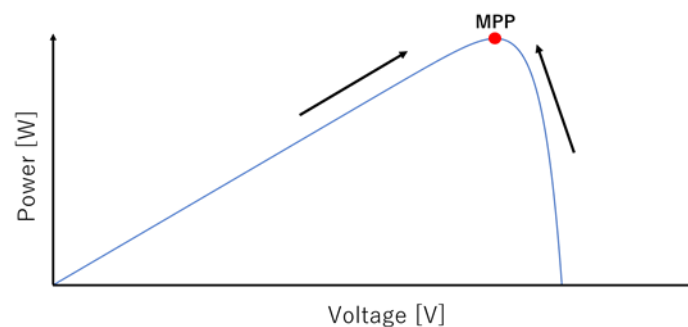


Fig. 17 PV characteristic curve [10]

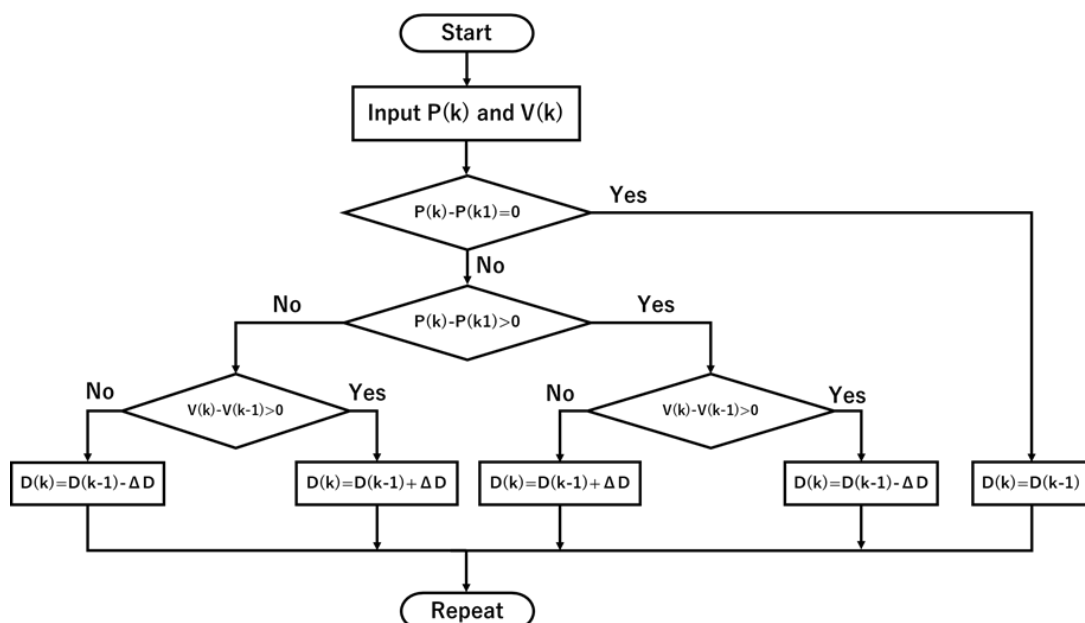


Fig. 18 P&O flow chart [10]

3.3. Modified P&O method

There are two concerns with the existing MPPT algorithms:

- 1) Most of them suffer from the drawback of being slow tracking, due to which the utilization efficiency is reduced;
- 2) Furthermore, intermittency and rapid irradiation, and temperature changes may cause the MPPT to be oscillating around one of the multiple local peaks of power.

To overcome the drawbacks mentioned above, more advanced controllers are needed to provide rapid control, and small oscillations once they reached the MPP and good performance under varying weather conditions.

To solve these problems, a variable perturbation step size method has been implemented to vary the perturbation step size via a tuning controller [3]. This requires precise adjustment using large values when the operating point is far from the MPP, and small values when it is close to the MPP. This results in high speed and low vibration MPP tracking performance.

However, even after solving the above problems, there is still power loss due to partial shading. To fix this drawback, several improvement methods have been proposed. They are based on more measurements of voltage and current to obtain more detailed data. Therefore, even if the loss due to partial shade can be avoided, a lot of time is spent on more complicated calculations.

3.4. Fuzzy logic concept

Fuzzy logic emerged in the fuzzy set context, introduced by Lotfi Asker Zadeh (1965) at the University of California, Berkeley [11]. It is a type of multi-valued logic, and its range is not limited from 0 to 1, like a truth value of the classical theory. In the crisp sets, if the ambient temperature is 20°C, it is judged as 0 (cold) when the border is at 25°C, as shown in Fig.5. But this method can't express how hot or cold it is. On the other hand, in the fuzzy sets, when the temperature is 28°C, it is judged to be 0.8 (hotness) or 0.2 (cold). Thus, Fuzzy logic can express linguistic variables by using values from 0 to 1. This is similar to the ways of human thinking. The fuzzy logic controller is based on this logic, and it is widely used for controlling electrical applications and machinery.

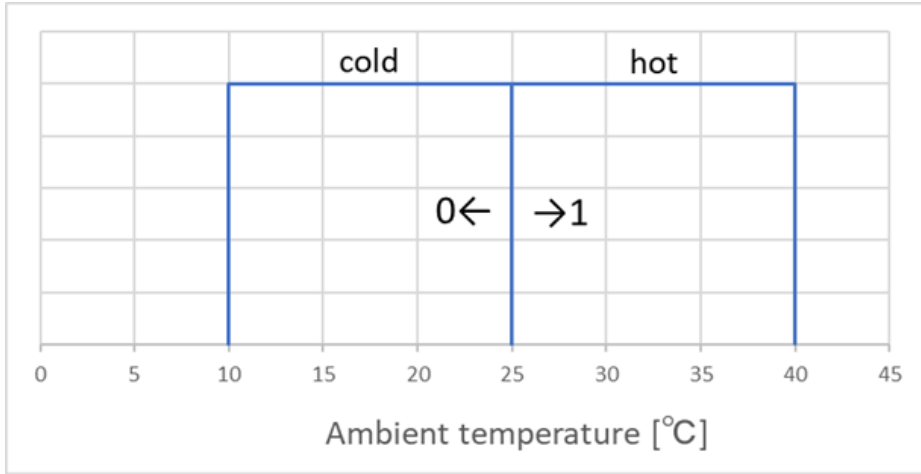


Fig. 19 Crisp sets

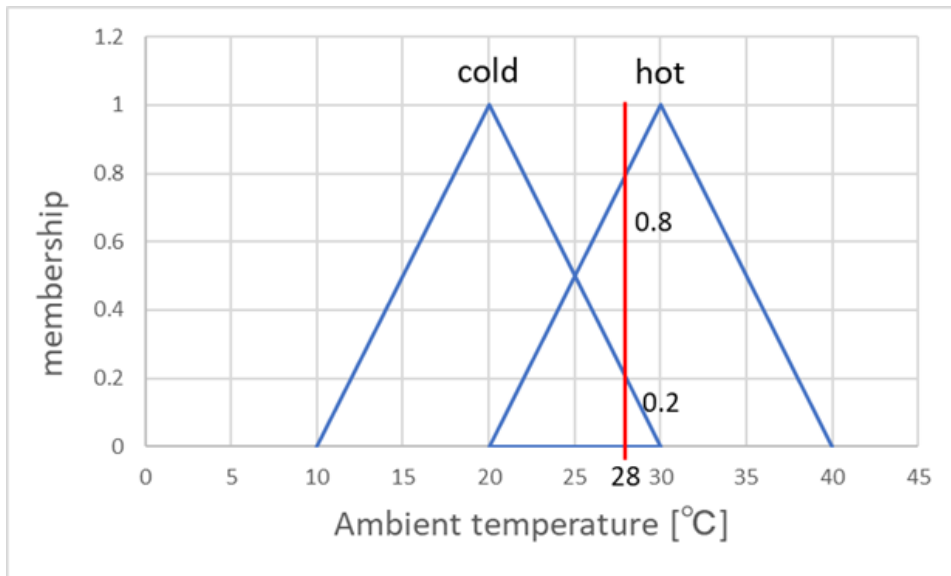


Fig. 20 Fuzzy sets

Chapter 4: MPPT based on Fuzzy Logic Control (FLC)

4.1. Fuzzy control for PV

The fuzzy logic controller is composed of three components, fuzzification, rule interface, and defuzzification [11]. Fig.21 shows the conceptual design of a FLC.

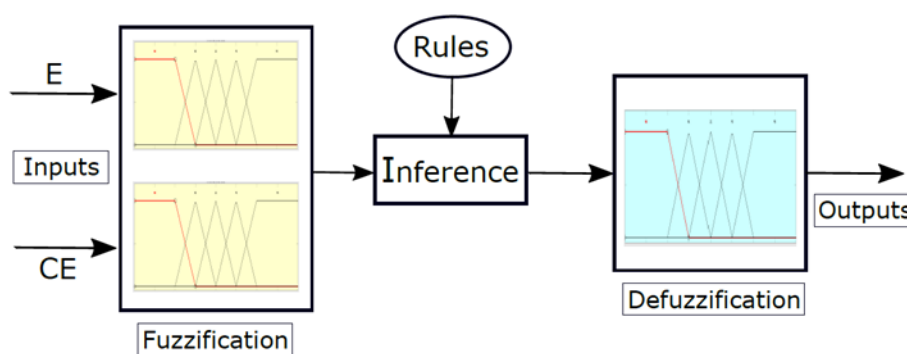


Fig. 21 Structure of fuzzy controller

Fuzzification

The FLC judges the OP position by using two inputs. These are the slope of the P-V curve's tangential line $\left(\frac{dP}{dV}\right)$ and displacement direction of the operating point $\left(\frac{d^2P}{dV^2}\right)$. These two inputs are expressed following equations, respectively.

$$E(k) = \frac{P(k) - P(k-1)}{V(k) - V(k-1)} \quad (26)$$

$$CE = E(k) - E(k-1) \quad (27)$$

Where, $P(k)$ and $V(k)$ are the power and voltage of the PV panel at sample time k .

These input values are converted to the linguistic variables through membership functions. Figure 22 and Figure 23 express membership functions for input values in this research. Linguistic variables are divided into five categories: NB (negative big), NS (negative small), ZE (zero), PS (positive small), PB (positive big). These membership functions in this figure are based on another paper [13].

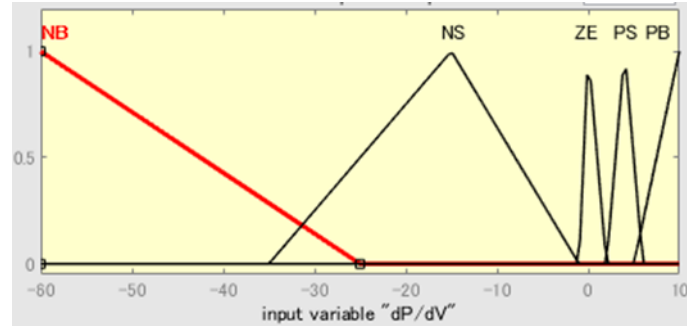


Fig. 22 Membership function for E ^[13]

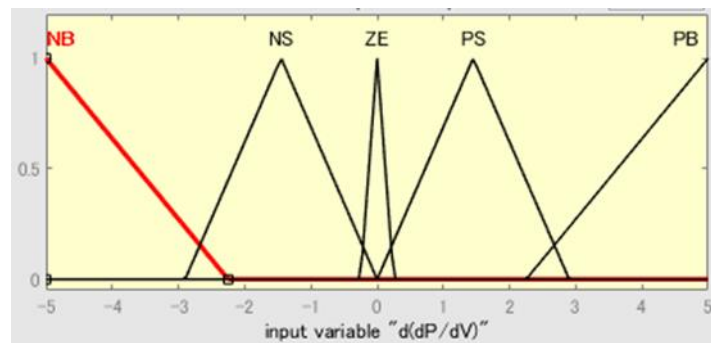


Fig. 23 Membership function for CE ^[13]

Fuzz rule

Table.1 shows the fuzzy rule used in this research [10]. These 25 rules determine fuzzy outputs. In the Power-Voltage curve, there are three regions, as shown in Fig.24. In region ①, $E(k)$ is positive. This indicates that the operating point is on the left side of MPP. To reach the MPP, the duty ratio should be decreased. For example, when $E(k)$ is PS and $CE(k)$ is NS, it means OP is approaching MPP from the left side. At this time, the fuzzy controller outputs ZE not to make oscillation. In region ②, $E(k)$ is zero, and OP is close to MPP. When $CE(k)$ is NB, the OP is moving towards the right side. And the controller outputs PS to stop the OP move. In region ③, $E(k)$ is negative. When $CE(k)$ is negative, the OP is getting away from MPP towards the right side. At this stage, the controller increases the duty cycle to bring the OP closer to MPP.

Table. 1 Fuzzy rule for PV

		CE				
		NB	NS	ZE	PS	PB
E	NB	ZE	PB	PB	PB	PB
	NS	PB	PB	PS	ZE	ZE
	ZE	PS	ZE	ZE	ZE	NS
	PS	ZE	ZE	NS	NB	NB
	PB	ZE	NB	NB	NB	ZE

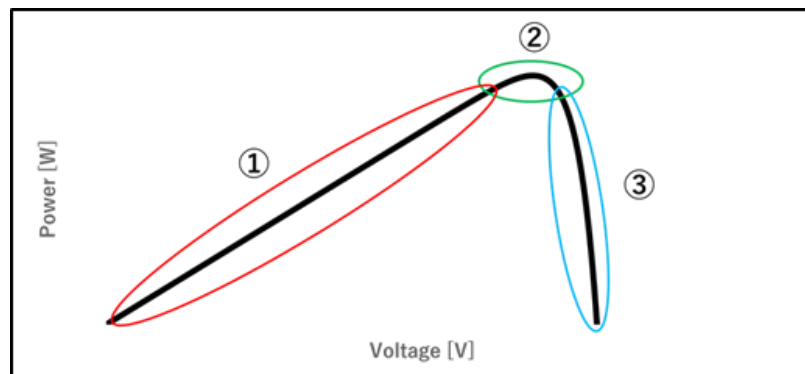


Fig. 24 Power-Voltage curve of PV module

Defuzzification

Finally, the outputs (ΔD) from the fuzzy controller are converted into numerical values, as shown in Fig.25, and duty cycle $D(k)$ is calculated by equation (28).

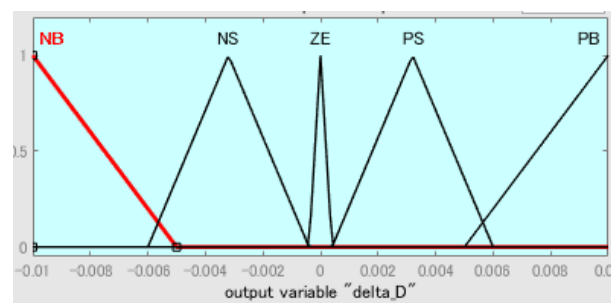


Fig. 25 Output membership function for ΔD ^[13]

$$D(k) = D(k - 1) + \Delta D \quad (28)$$

4.2. Fuzzy control for wind turbine

The following equations represent inputs for the fuzzification in the wind turbine. The wind generator is more complicated than the PV system, and it is difficult to figure out the inside mechanism. Therefore, the fuzzy logic controller for wind generators is based on power change and voltage change to make them simple. The same equation calculates output ΔD with PV's. Fig.26, Fig.27 and Fig.28 show membership functions for $E(k)$, $CE(k)$ and ΔD , respectively. Table2 represents the fuzzy rules.

$$E(k) = P(k) - P(k - 1) \quad (29)$$

$$CE(k) = V(k) - V(k - 1) \quad (30)$$

$$D(k) = D(k - 1) + \Delta D \quad (31)$$

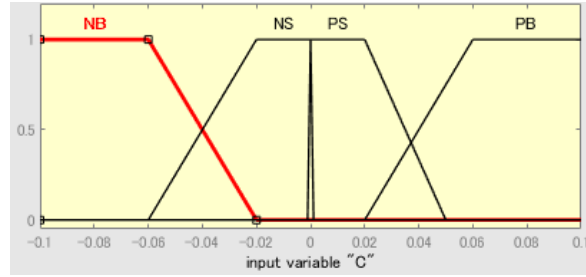


Fig. 26 Input membership for *C*

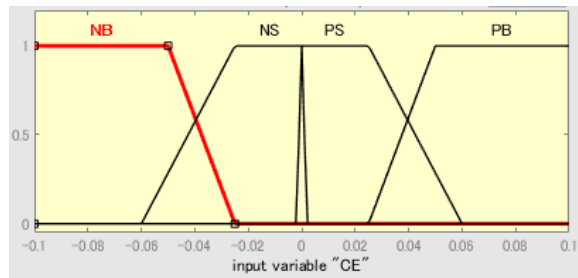


Fig. 27 Input membership for *CE*

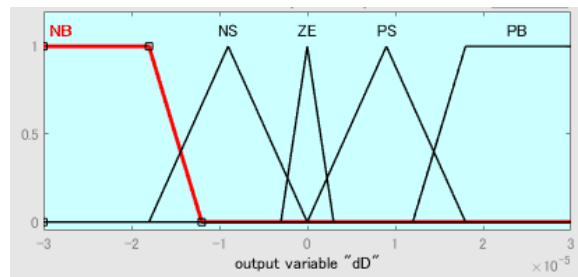


Fig. 28 Output membership function for ΔD

Table. 2 Fuzzy rule for WECS

		CE			
		NB	NS	PS	PB
E	NB	NB	NS	PS	PB
	NS	NS	NS	PS	PS
	PS	NS	ZE	ZE	PS
	PB	NS	ZE	ZE	PS

Chapter 5: Simulation model

5.1. Solar PV simulation model

Figures 29 and figure 30 show the whole PV Simulink model, including P&O and FLC MPPT systems. The technical specification of the solar panel used in this study is given in Table.3. Figure 31 shows the schematic diagram of the buck converter. The DC-DC converter is used as an impedance matching system to track the MPP [5]. Buck converter switch ON and OFF to adjust the output voltage by referring to the duty cycle from the MPPT, following the MPP voltage.

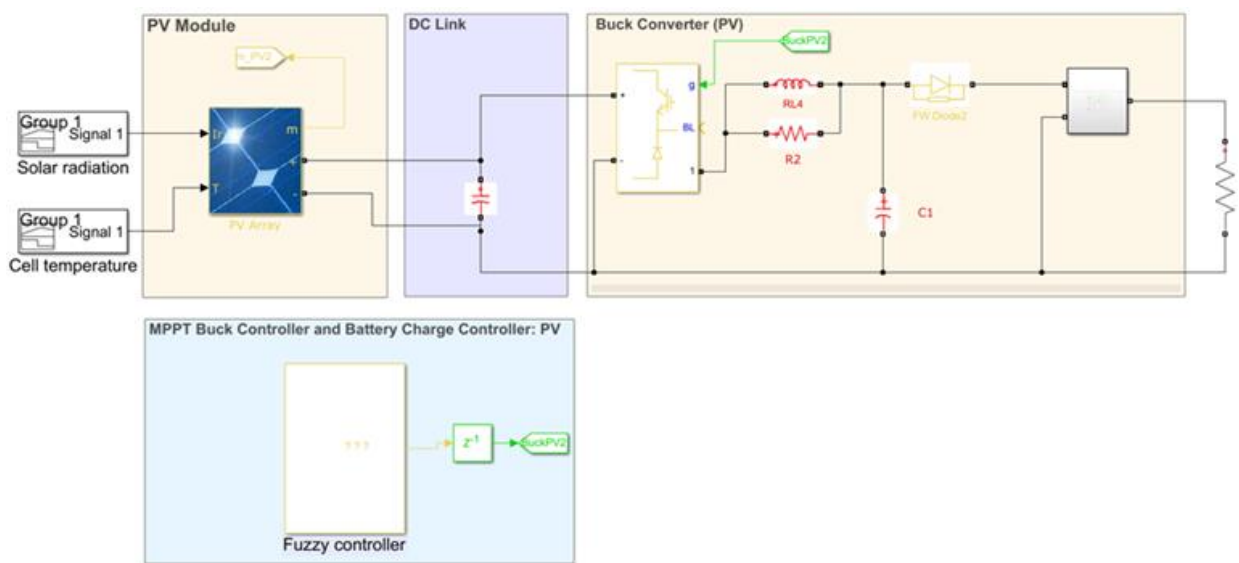


Fig. 29 PV Simulink model

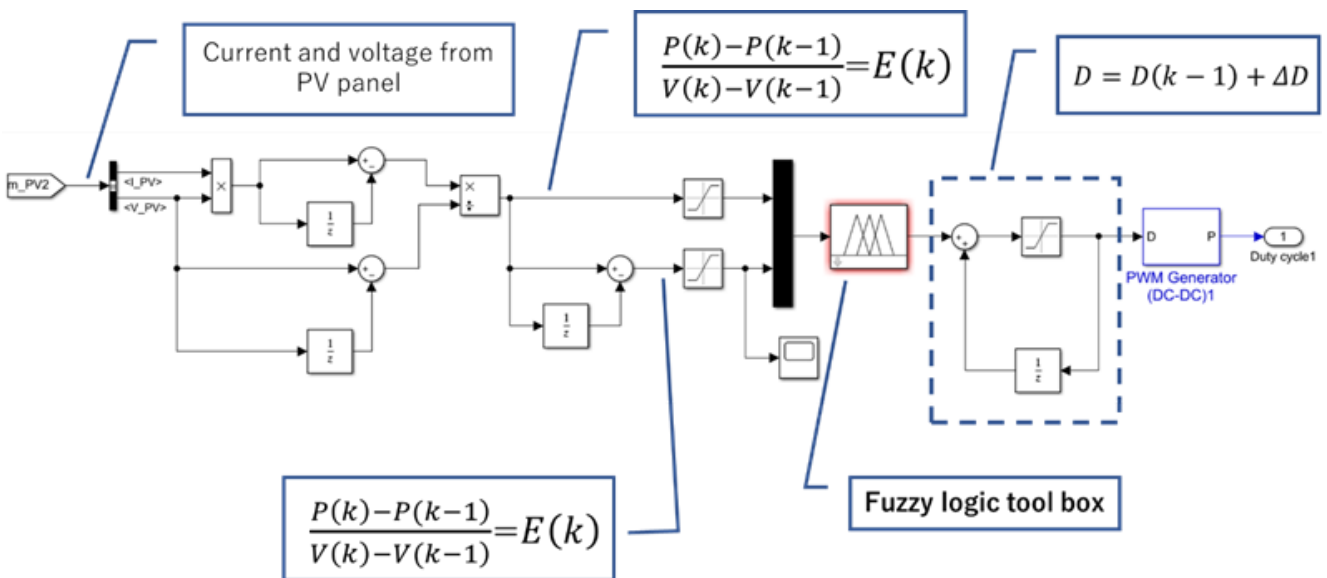


Fig. 30 Fuzzy controller Simulink model

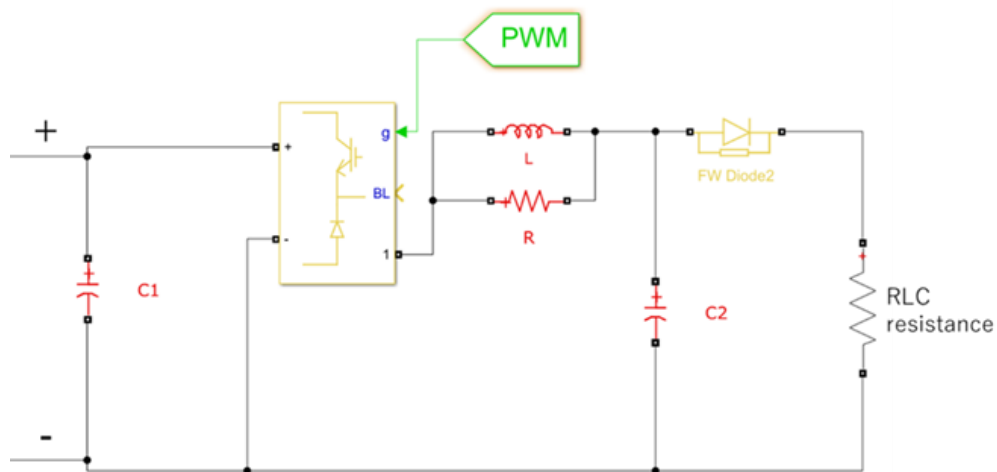


Fig. 31 Schematic diagram of the buck converter

Table. 3 Specs of the solar panel

Maximum Power [W]	160
Voltage at MPP [V]	17.9
Current at MPP [A]	8.94
Open circuit voltage [V]	21.6
Short circuit current [A]	9.47
Temperate coefficient of Isc [%/°C]	0.10±0.01
Temperate coefficient of Voc [%/°C]	- (0.38 ±0.01) %/ °C
The number of cells on the PV panel	36

Table.4 shows the technical parameters of the buck converter. In this buck converter, an IGBT buck converter is installed in each photovoltaic and wind power generation system. In this model, the PWM signal is controlled by combining IGBTs and diodes, followed by inductors, freewheeling diodes, and capacitors. The PWM generator samples at a frequency of 30000 Hz [5].

Table. 4 Parameter of the buck converter

Capacitance (C1)	2.2 [mF]
Capacitance (C2)	2.2[mF]
Resistance (R)	10000e3 [Ω]
Inductance (L)	3[mH]

5.2. Solar PV measurement system and model validation

In this study, the experimental system is installed at the Kyushu University Chikushi Campus, which serves as a test pilot for system implementation. The experimental setup is located on the campus in Kasuga City, Fukuoka Prefecture, Japan. Fig.32 shows the installed experimental setup. They are configured as a single HRES and include solar panels, wind turbine generator, lead-acid batteries, inverter, and controller. Tables.5 and 6 show the performance of the battery and battery charge controller.

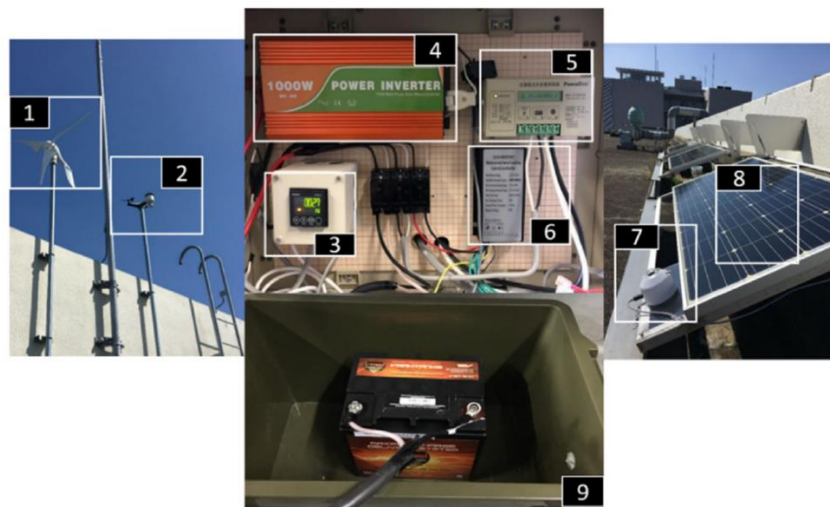


Fig. 32 (1) Wind turbine, (2) Weather measurement station, (3) Datalogger, (4) Inverter, (5) PV DC converter and controller,(6) Wind DC converter and controller, (7) Pyranometer, (8) PV module, (9) Battery [5]

Table. 5 Battery parameters

Type	Lead-acid
Fully charge voltage	14 V
20Hr capacity	30 AH
RC (min)	55
CCA	280
Charging current	2–10 A
Charging voltage	14.4–14.9 V
Float voltage	13.5–13.8 V

Table. 6 Battery charge controller parameters

Float voltage setpoint	13.6 V
Buck voltage setpoint	14.5 V
DC-DC Charge controller	Discrete-time-PI based
Proportional (p)	5
Integral (I)	150
Anti-windup gain	1
Control action upper limit	1
Control action lower limit	0
Sample time	Inherited
Time constant voltage filter	0.0001

In addition to Fig.32, a new measuring instrument was introduced in this study, which consists of the following three parts.

- Incident solar radiation on the PV tilted surface, using Pyranometer
- PV Cell temperature measurement, using the surface thermocouple
- I-V curve measuring and analysis

All of the above measure data will be used to validate the results of the simulation model.

Incident solar radiation on the tilted surface

Pyranometer was used to measure the incident solar radiation on the tilted PV surface. The solar radiation is measured as voltage [mV] by pyranometer. Collected data are converted to W/m² by equation (32) [14]. Fig.33 shows the setup system of the pyranometer.

$$G = \frac{S}{0.00692} \times 1000 \quad (32)$$

G: Solar radiation [W/m²]

S: measured solar radiation by pyranometer [mV]

Table. 7 Pyranometer specification [14]

MS-40C Pyranometer	
Wavelength range	285~3000 nm
Sensitivity	Approx. 7.00 $\mu\text{V}/\text{W}/\text{m}^2$
Output	Analog (mV)
Response time 95%	<18 Sec.
Zero off-set a) 200W/m ²	<12 W/m ²
Zero off-set b) 5K/hr	± 5 W/m ²
Non-stability change/1 year	<1.5 %
Non-linearity at 1000W/m ²	± 1 %
Directional response at 1000W/m ²	± 20 W/m ²
Spectral error	± 1 %
Temperature response -10°C to 40°C	<3 %
Temperature response -20°C to 50°C	<4 %
Tilt response at 1000W/m ²	± 1 %
Impedance	140 Ω
Operating temperature range	-40~80°C
Ingress protection IP	IP67

Fig.34 also shows the hourly data of solar radiation measured by the solar radiation meter from April to October.

**Fig. 33 Pyranometer**

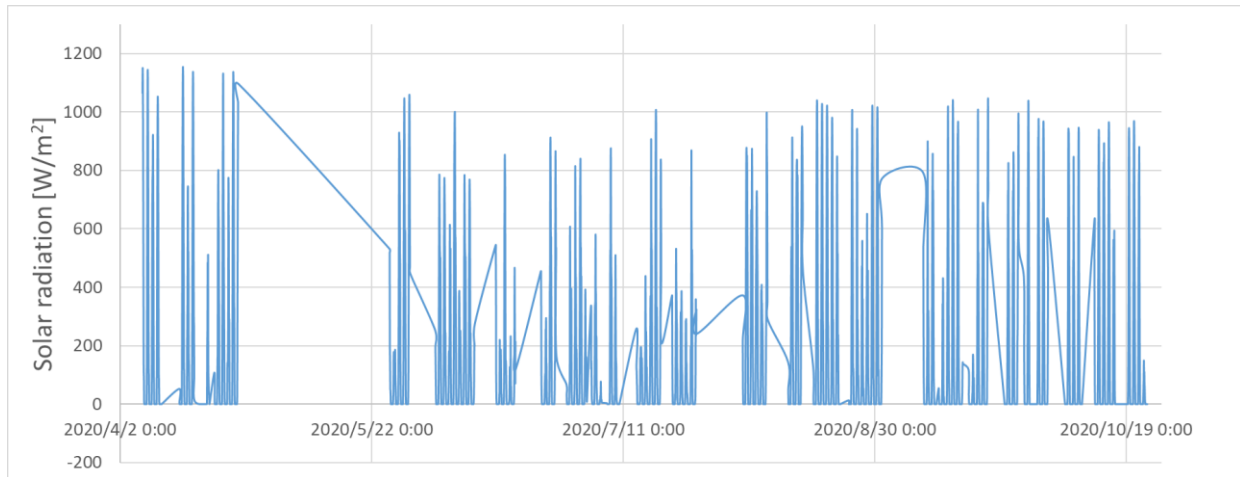


Fig. 34 Measured data on solar radiation

Cell temperature measurement

The cell temperature affects PV efficiency. To collect cell temperature data, a surface thermocouple was used with the technical specification given in Fig.35. The cell temperature can be calculated, using the following empirical formula [15].

$$T_{cell} = T_{air} + \frac{NOCT - 20}{80} S \quad (33)$$

T_{cell} : Cell temperature [°C]

T_{air} : Ambient temperature [°C]

$NOCT$: Nominal operating cell temperature = 44 [°C]

S : Incident solar radiation [mW/cm²]

Fig.36 shows the comparison between measured and calculated cell temperature from 9 to 11 in June 2019. Although measurement data is affected by wind and rain, there is good agreement between the measured and estimated values.

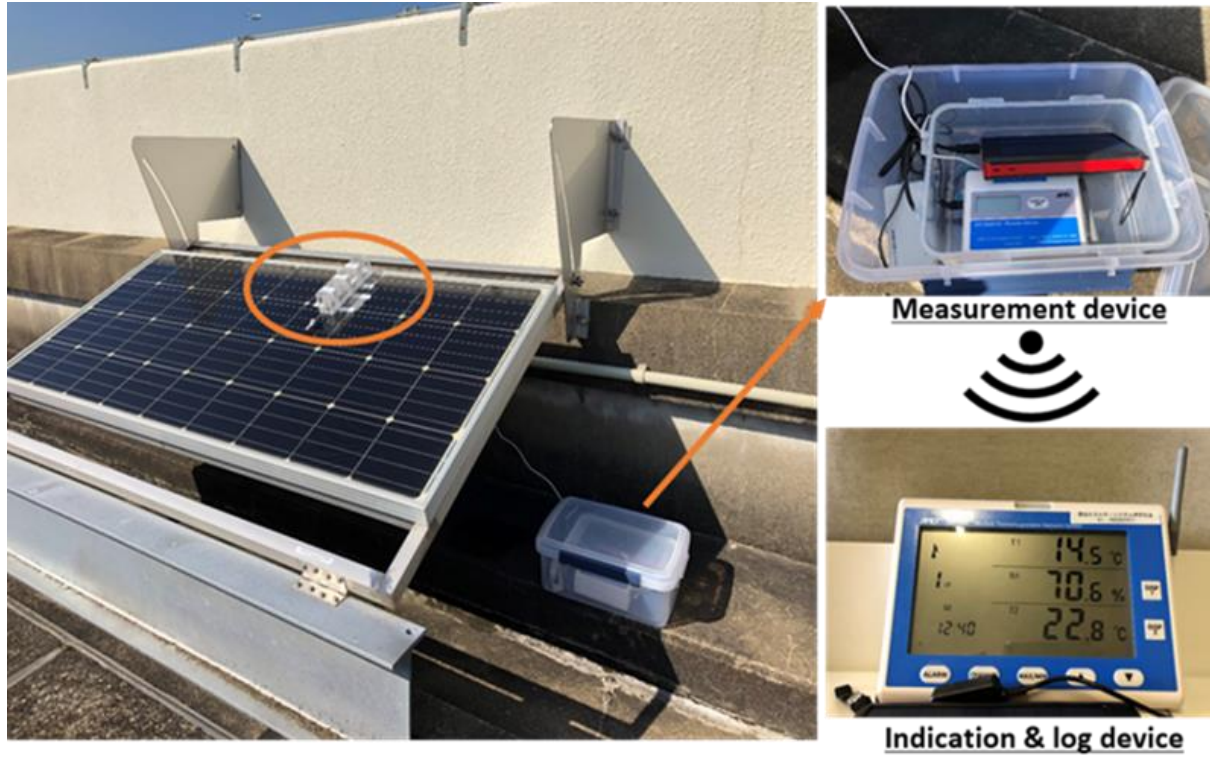


Fig. 35 Cell temperature measurement system

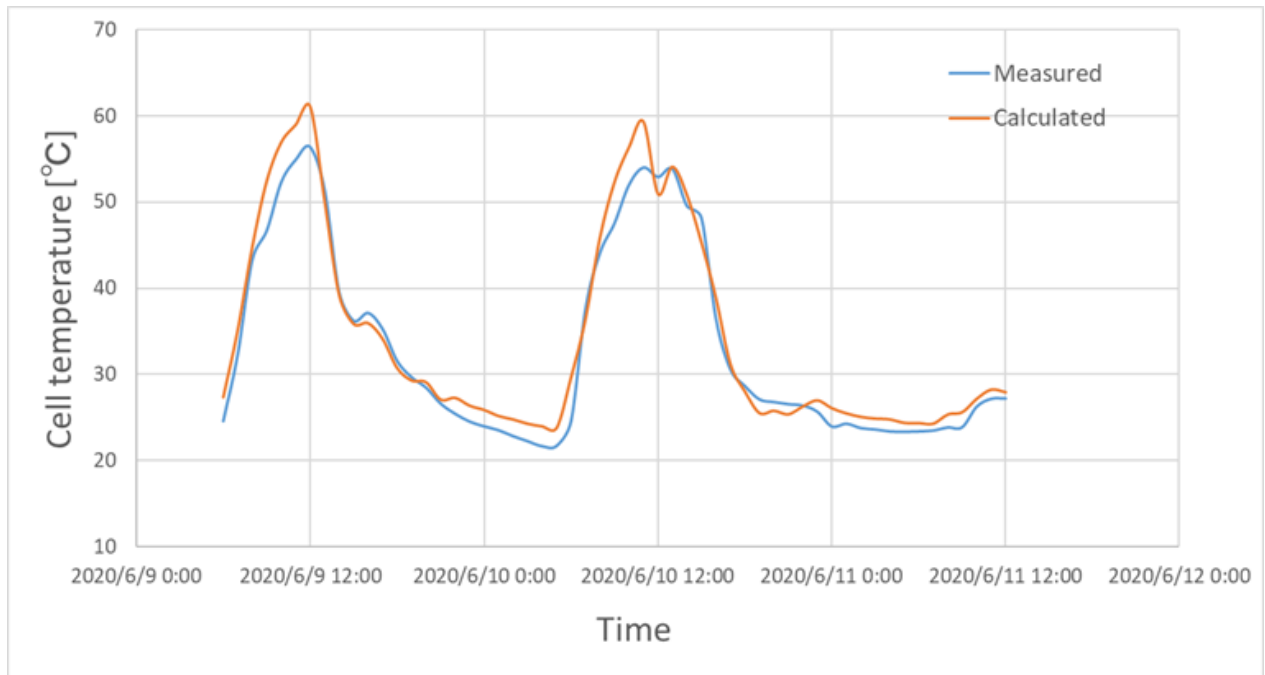


Fig. 36 Comparison of measured and calculated cell temperature

I-V curve measurement

Fig.37 shows the PV power analyzer used in this study. A necessary part of estimating a PV panel's power output in a simulation model is to validate its results. The PV power analyzer was used to compare the actual PV panel power curve with the simulation one to see if they match. This instrument can measure currents up to 200A, but an error will occur if the current exceeds that limit. Therefore, it is necessary to take into account the power output of the panels and choose the optimal time of day for solar radiation that will not exceed it.



Fig. 37 PV power measurement device

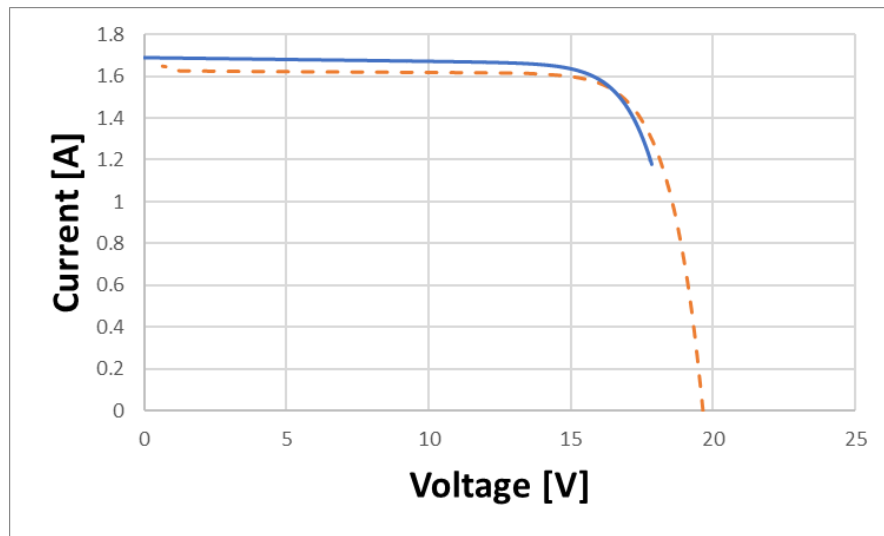
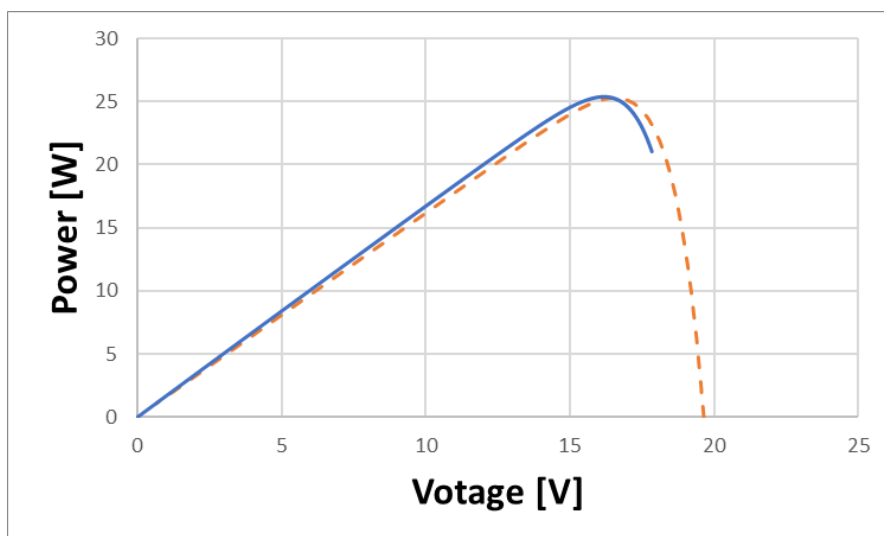
5.3. PV simulation model validation

In this research, two sizes of solar panels (50 W and 160 W) were considered for the validation of the simulation results. The technical specifications of both panels are given in Table.8. In order to validate the simulation results, the I-V curves were plotted based on the real measured data from the I-V analyzer and the simulation results, which are represented in Fig.38 to Fig.41

. Since in the simulation model, the MPPT controller moves the OP to the MPP; therefore, each curve of the simulation result is cut off in the middle. In addition, the output values are higher than the actual measured values because the simulation model is equipped with fuzzy control, and furthermore, panel degradation is not taken into account.

Table. 8 160W and 50W PV panel spec

	160W PV panel	50W PV panel
Maximum Power [W]	160	50
Voltage at MPP [V]	17.9	18.3
Current at MPP [A]	8.94	2.9
Open circuit voltage [V]	21.6	21.8
Short circuit current [A]	9.47	3.1
The number of cells	36	33

**Fig. 38 I-V curve of the 50W solar panel (Measured at 12:40 on September 23, 2020)****Fig. 39 P-V curve of the 50W solar panel (Measured at 12:40 on September 23, 2020)**

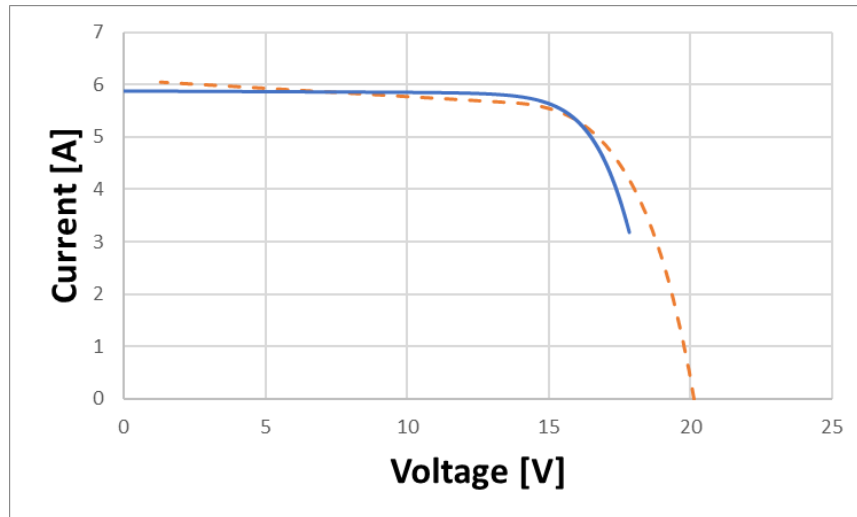


Fig. 40 I-V curve of the 160W solar panel (Measured at 12:45 on September 23, 2020)

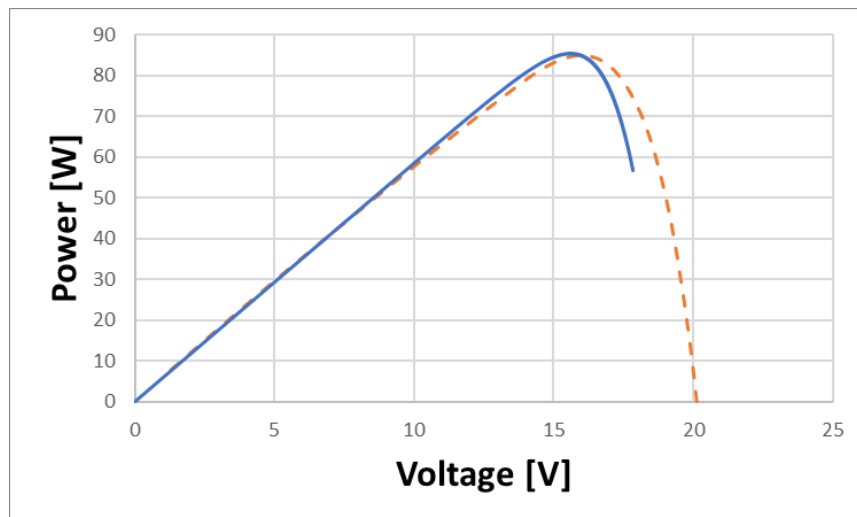


Fig. 41 P-V curve of the 160W solar panel (Measured at 12:45 on September 23, 2020)

The comparison between the measured data by the analyzer and estimated results from the simulation is shown in Table.9 and Table.10, emphasizing the accuracy of the simulation results.

**Table. 9 Measurement and simulation results for 50W solar panel
(Measured at 12:40 on September 23, 2020)**

	measured	simulation
Isc [A]	1.66	1.69
Voc [V]	19.66	
Pmax [W]	25.29	25.38

**Table. 10 Measurement and simulation results for 160W solar panel
(Measured at 12:45 on September 23, 2020)**

	measured	simulation
Isc [A]	6.09	5.88
Voc [V]	20.12	
Pmax [W]	85.04	85.48

5.4. Wind power simulation

Fig.42 shows the wind turbine generator in the Simulink model, which consists of the wind turbine itself, back converter, and MPPT controller. A battery is also connected to the load part in parallel in order to keep the voltage applied to the load constant and prevent errors that may occur during the simulation. The technical specification of the wind turbine generator used in this simulation is shown in Table.11. Furthermore, the configuration of the buck converter is the same as that of the solar, but the values of each element are different, and these values are shown in Table.12.

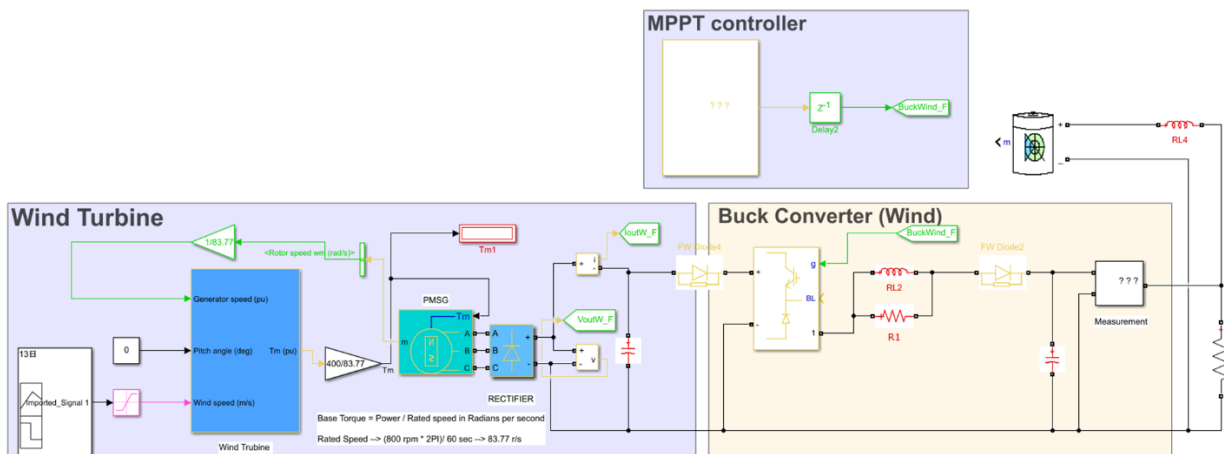


Fig. 42 Wind generator Simulink model

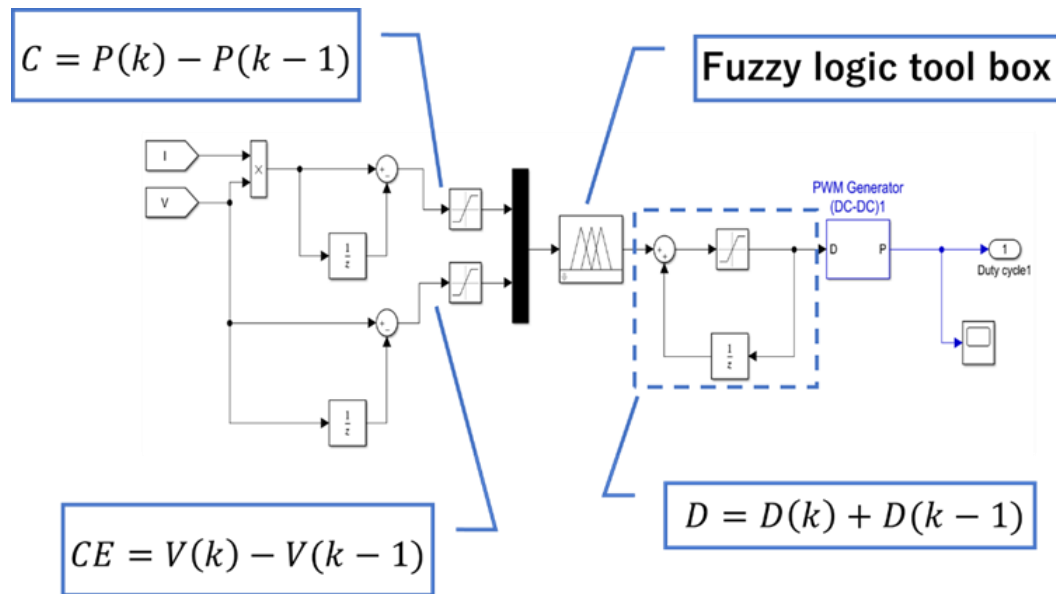
Table. 11 Wind generator parameters

Rated power	400 W
Rated voltage	12 V
Start-up wind speed	2.5 m/s
Rated wind speed	10.5 m/s
Maximum wind speed	35 m/s
Rated rotation speed	800 rpm
Fan blade quantity	3
Rotor blades diameter	1.2 m

Table. 12 Parameter of the buck converter

Capacitance (C1)	0.55 [mF]
Capacitance (C2)	2.2[mF]
Resistance (R)	10000e3 [Ω]
Inductance (L)	1.5[mH]

Fig.43 shows the MPPT controller's details, where the fuzzy controller determines the appropriate output value ΔD based on the two input values mentioned in chapter 6.2.

**Fig. 43 Simulink model of the fuzzy controller for wind generator**

5.5. Simulation results

Fig.44 shows incident solar irradiance on the PV panel and cell temperature at 10 am on April 14 in 2020. Fig.45 shows the comparison between the P&O-based MPPT and the proposed FLC-based MPPT in this research for a short period of ten minutes simulation on this sunny day. As shown in this figure, the FLC-based MPPT extracts higher power with lower oscillation than the P&O controller. The hourly estimation of the output power from the PV panel was compared between the FLC and P&O in Table.13. The better performance of the FLC is more evident at the higher levels of solar irradiation.

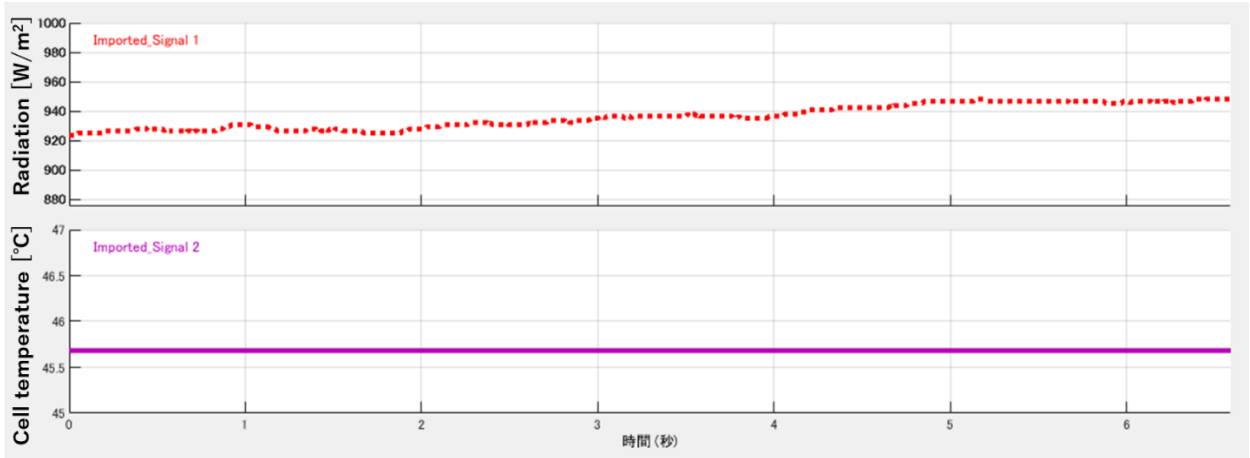


Fig. 44 Solar irradiance and cell temperature at 10am on April 14 in 2020

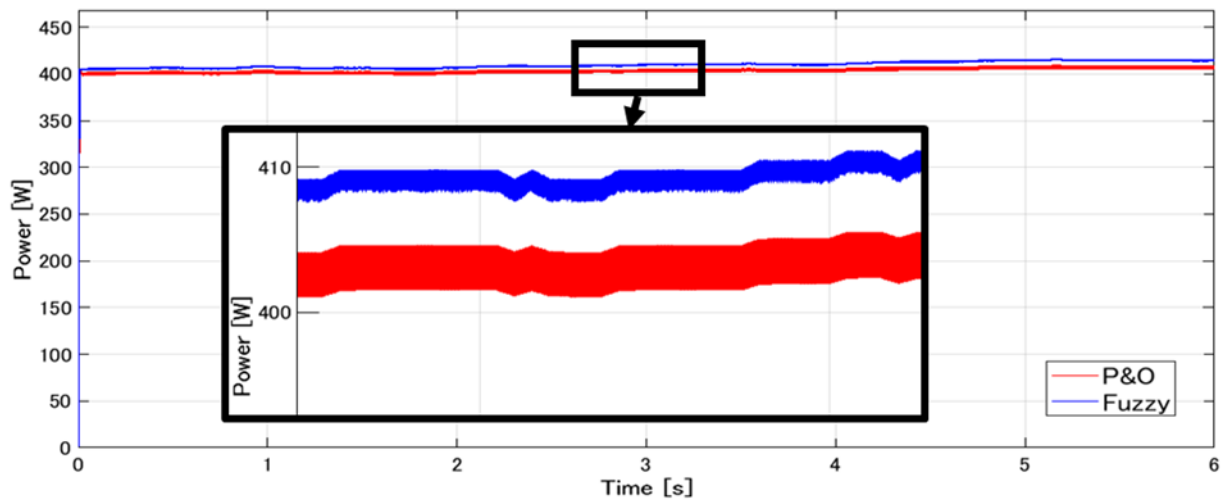


Fig. 45 PV power of the fuzzy and P&O on April 14 in 2020

Table. 13 1day simulation results on April 14

	Solar radiation [W/m ²]	Power (Fuzzy) [Wh]	Power (P&O) [Wh]	P&O power [Wh](>=70W/m ²)	Difference [Wh]	Difference [Wh](>=70W/m ²)	
6:00	16.2	0.6	2.3	0.0	-1.70	0.00	
7:00	59.4	8.9	17.6	0.0	-8.67	0.00	
8:00	98.5	44.8	42.8	42.8	2.02	2.02	
9:00	773.0	344.7	335.0	335.0	9.72	9.72	
10:00	936.1	409.2	402.9	402.9	6.28	6.28	
11:00	1010.6	436.9	415.4	415.4	21.57	21.57	
12:00	1030.3	447.3	424.6	424.6	22.70	22.70	
13:00	958.6	420.4	410.8	410.8	9.56	9.56	
14:00	830.2	372.4	372.5	372.5	-0.07	-0.07	
15:00	627.9	287.4	283.6	283.6	3.81	3.81	
16:00	387.6	179.9	175.1	175.1	4.81	4.81	
17:00	87.1	39.8	35.4	35.4	4.40	4.40	
18:00	38.5	2.4	8.8	0.0	-6.44	0.00	
19:00	0.0	0.0	0.0	0.0	0.00	0.00	
		Total		2898.1	67.98	84.79	
						Total benefit [%]	2.93

The results of the simulations for different time periods and climatic conditions are shown below. The data for cloudy days is from July 17, 2020, and the data for rainy days is from October 22, 2020. The comparison of hourly power generation by P&O controller and fuzzy controller for these two days is summarized in Tables.14 and 15. Fig.49 shows that the power based on the fuzzy controller is significantly below the P&O controller and oscillates. This means that the fuzzy controller could not find the maximum power point because the P-V curve slope was extremely small due to the low solar radiation.

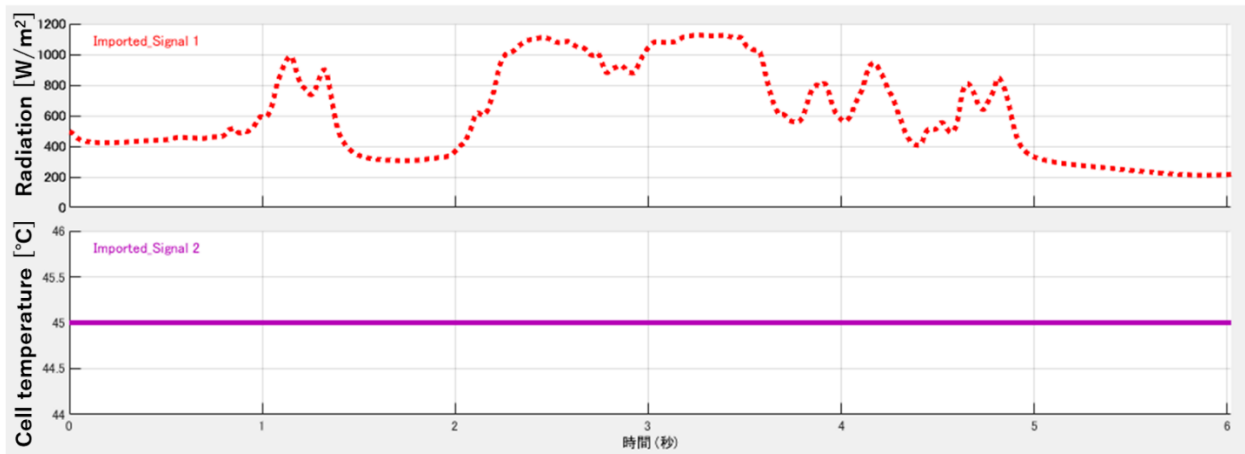


Fig. 46 Solar irradiance and cell temperature at 10am on July 17 in 2020

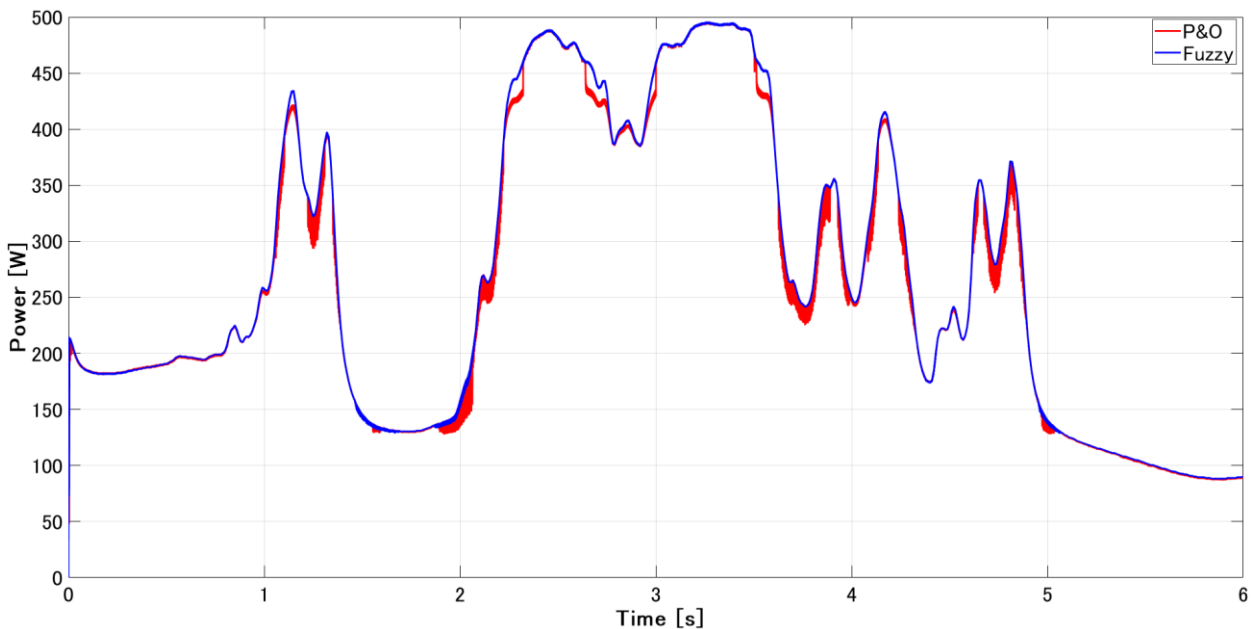


Fig. 47 PV power of the fuzzy and P&O on July 17 in 2020

Table. 14 1day simulation results on July 17

	Solar radiation [W/m ²]	Power (Fuzzy) [Wh]	Power (P&O) [Wh]	P&O power [Wh](≥70W/m ²)	Difference [Wh]	Difference [Wh](≥70W/m ²)
6:00	41.3	7.3	9.7	0.0	-2.33	0.00
7:00	100.2	44.4	43.5	43.5	0.89	0.89
8:00	628.8	275.8	268.9	268.9	6.96	6.96
9:00	844.2	362.5	361.7	361.7	0.75	0.75
10:00	614.6	267.3	264.3	264.3	3.03	3.03
11:00	437.7	194.9	192.1	192.1	2.86	2.86
12:00	804.2	343.2	337.9	337.9	5.32	5.32
13:00	445.6	186.1	183.4	183.4	2.67	2.67
14:00	134.4	56.8	54.6	54.6	2.22	2.22
15:00	230.1	101.7	101.2	101.2	0.54	0.54
16:00	121.9	52.5	51.7	51.7	0.79	0.79
17:00	47.4	9.8	12.5	0.0	-2.73	0.00
18:00	44.8	3.0	11.2	0.0	-8.23	0.00
19:00	0.0	0.0	0.0	0.0	0.00	0.00
Total				1859.17	12.76	26.04
Benefit [%]						1.40

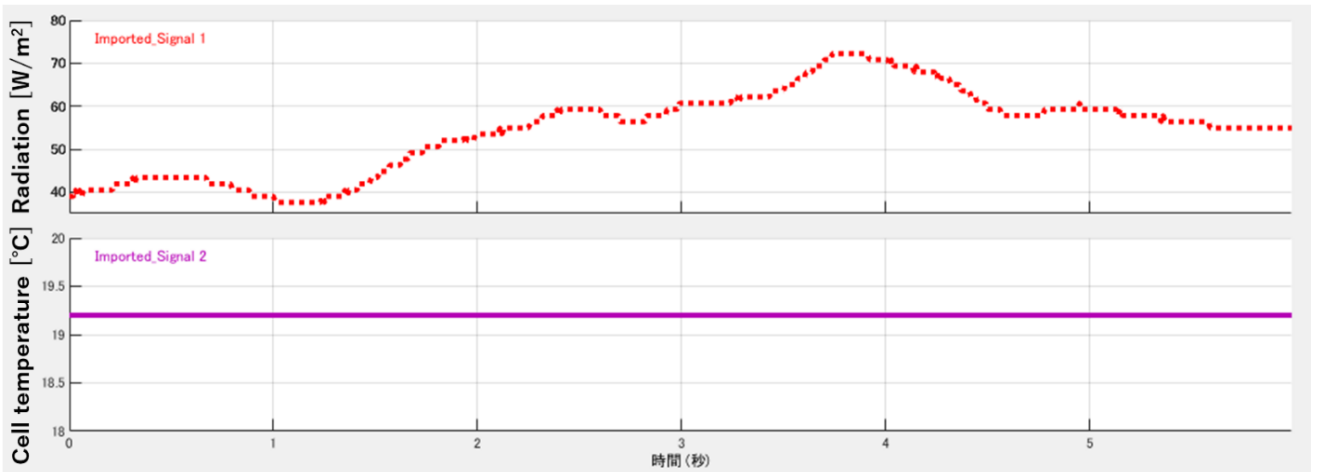


Fig. 48 Solar irradiance and cell temperature at 10am on October 22 in 2020

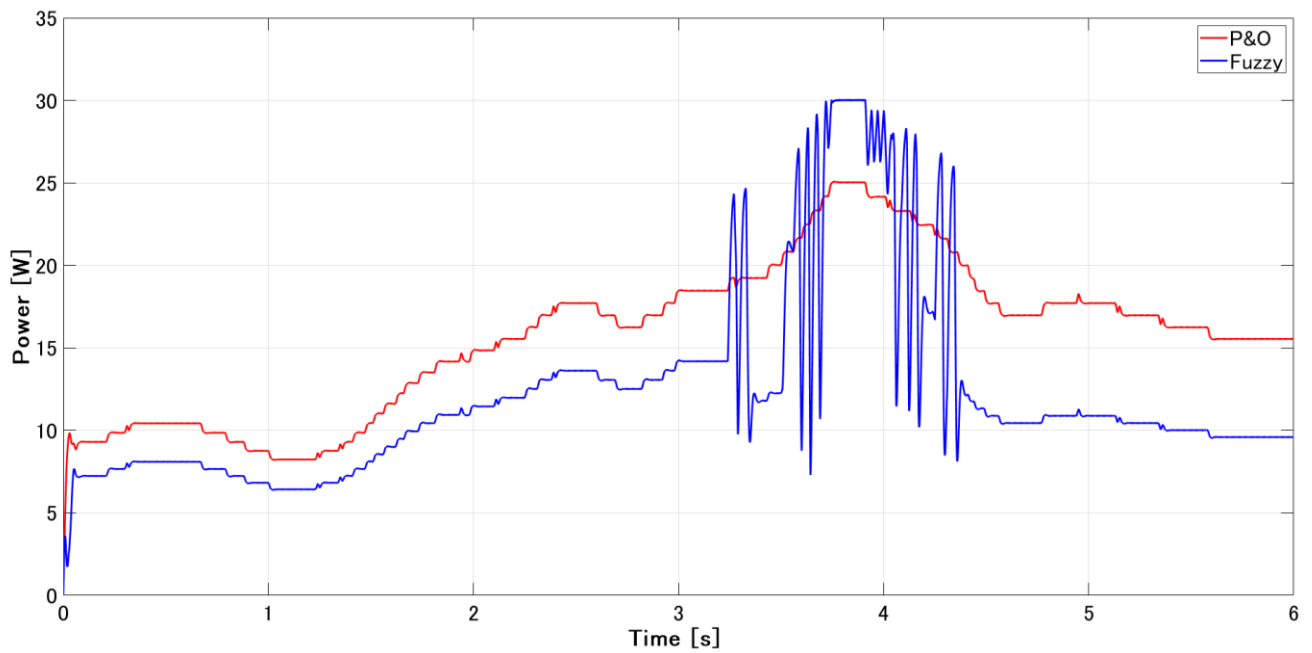


Fig. 49 PV power of the fuzzy and P&O on October 22 in 2020

Table. 15 1day simulation results on October 22

	Solar radiation [W/m ²]	Power (Fuzzy) [Wh]	Power (P&O) [Wh]	P&O power [Wh]($\geq 70\text{W/m}^2$)	Difference [Wh]	Difference [Wh]($\geq 70\text{W/m}^2$)	
6:00	0.00	0.00	0.00	0.00	0.00	0.00	
7:00	13.45	0.45	1.91	0.00	-1.46	0.00	
8:00	39.60	2.45	9.07	0.00	-6.62	0.00	
9:00	81.57	35.51	31.14	31.14	4.37	4.37	
10:00	54.59	12.15	15.71	0.00	-3.56	0.00	
11:00	39.09	1.84	8.93	0.00	-7.09	0.00	
12:00	80.98	31.77	31.62	31.62	0.15	0.15	
13:00	71.15	25.19	24.69	24.69	0.50	0.50	
14:00	64.52	16.11	20.65	0.00	-4.54	0.00	
15:00	20.13	0.72	3.20	0.00	-2.49	0.00	
16:00	8.40	0.35	0.95	0.00	-0.60	0.00	
17:00	0.00	0.00	0.00	0.00	0.00	0.00	
18:00	0.00	0.00	0.00	0.00	0.00	0.00	
19:00	0.00	0.00	0.00	0.00	0.00	0.00	
Total					87.4	-21.3	5.03
Benefit [%]							5.75

The simulation model was carried out, considering a sunny, cloudy, and rainy day in each month (see Table.16).

Table. 16 Date the simulation was performed

Sunny day	Cloudy day	Rainy day
1-Jan	13-Jan	22-Jan
4-Feb	7-Feb	12-Feb
20-Mar	22-Mar	28-Mar
14-Apr	15-Apr	19-Apr
1-May	25-May	26-May
8-Jun	4-Jun	25-Jun
16-Jul	17-Jul	6-Jul
29-Aug	28-Aug	7-Aug
14-Sep	20-Sep	12-Sep
20-Oct	8-Oct	22-Oct
5-Nov	19-Nov	18-Nov
12-Dec	29-Dec	22-Dec

The simulation results for an entire period of one year are reported in Table.17. The results revealed a potential of 2% extra power generation from the proposed HRES, using the FLC-based MPPT system. According to the results, by implementing the FLC-based MPPT system, *about 26.2 kWh/y excess electricity can be extracted from each KW installed capacity of solar panels n the Chikushi campus.*

Table. 17 1year simulation results

	P&O power [kWh]	Fuzzy power [kWh]	Power difference [kWh]	saving [%]
January	33.41	34.16	0.76	2.27
February	38.55	39.37	0.82	2.13
March	52.92	54.47	1.55	2.94
April	66.05	67.92	1.87	2.83
May	62.33	63.73	1.40	2.24
June	66.27	67.54	1.27	1.92
July	26.20	26.57	0.37	1.42
August	54.01	55.02	1.01	1.86
September	52.68	53.91	1.24	2.35
October	59.61	60.69	1.07	1.80
November	49.67	50.59	0.92	1.84
December	15.79	16.09	0.29	1.86
Total	577.49	590.06	12.57	2.18

Fig.50 and Fig.52 show the wind speed for 24 hours in Fukuoka city on April 1 in 2020. The comparison between the FLC and P&O MPPT for the wind turbine is shown in Fig.51 and 53. As shown in these figures, there are almost no differences between fuzzy and P&O controller results for the wind power generator. Although the proposed FLC offers excellent performance in controlling solar panels, it doesn't significantly improve the wind turbine's maximum power, particularly at low wind speed. This is because the wind control system includes mechanical (pitch control) and electrical power sections, but only the electrical section was considered in this research.

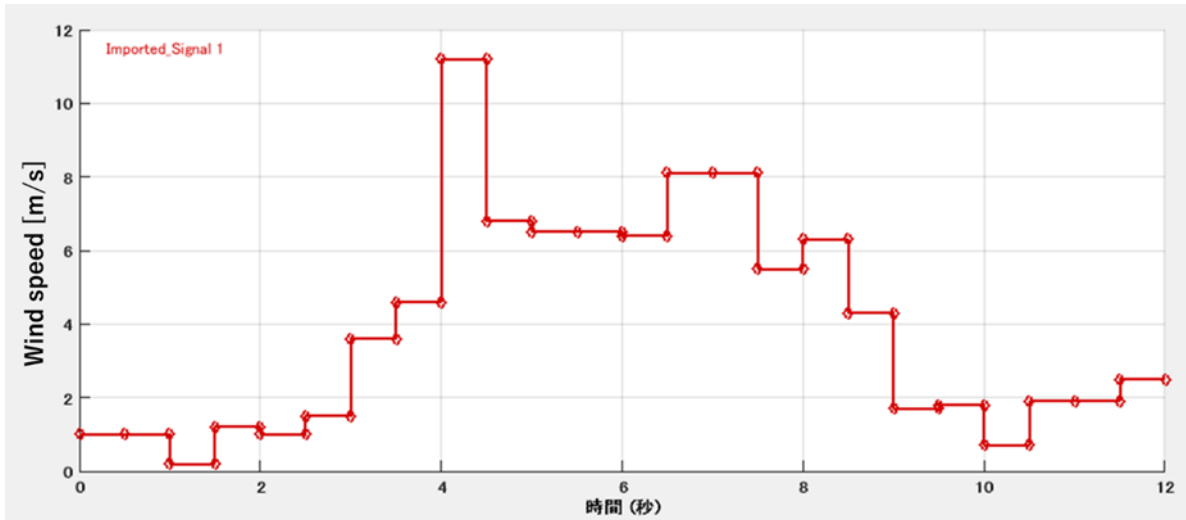


Fig. 50 Wind speed on April 1, 2020

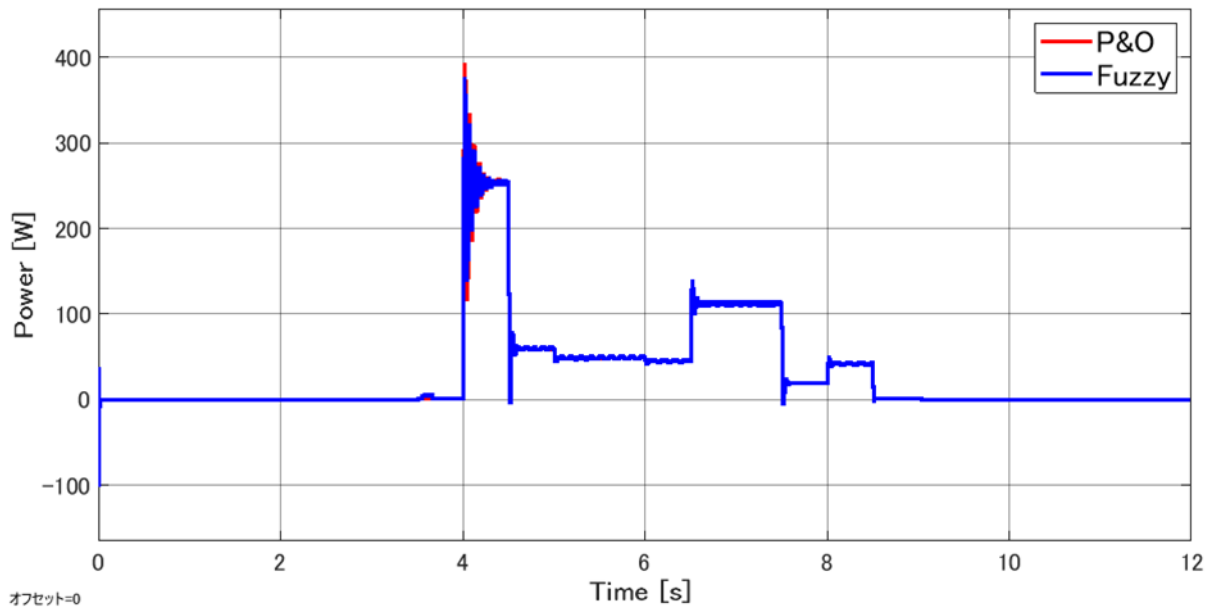


Fig. 51 Power generated by wind turbine

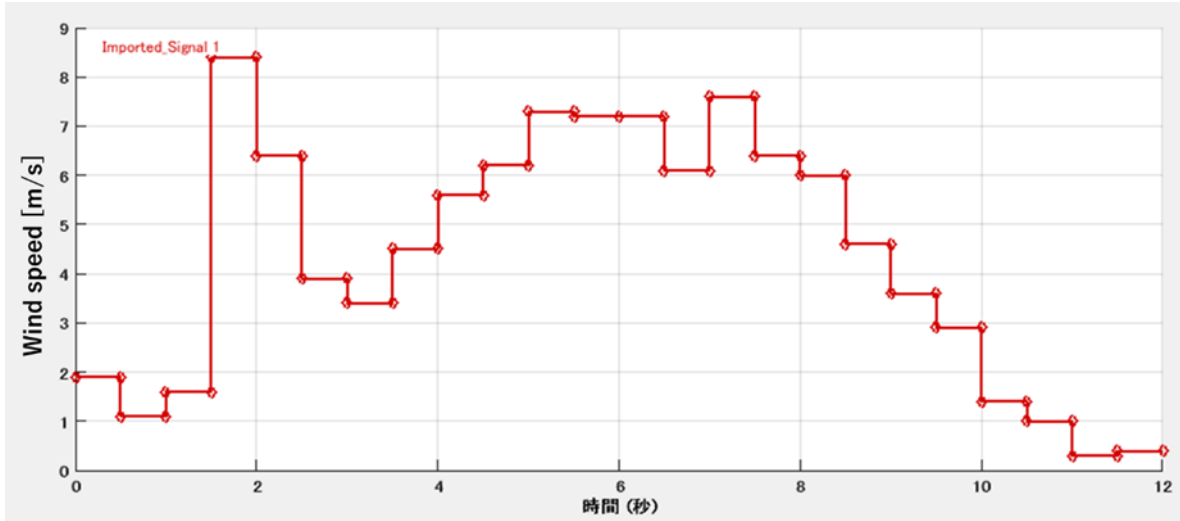


Fig. 52 Wind speed on April 2, 2020

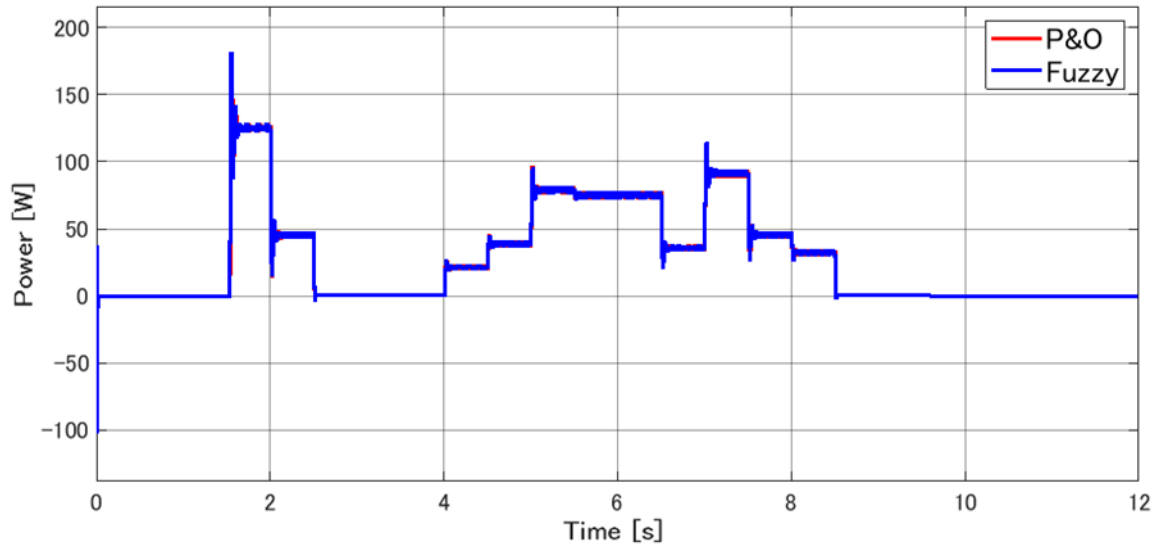


Fig. 53 Power generated by wind turbine

Chapter 6: Techno-economic analysis of the HRES

HOMER Pro is used for techno-economic analysis in this research. HOMER software was developed by NREL (National Renewable Energy Laboratory). This software enables the optimal design and sizing of hybrid renewable energy systems by performing a techno-economic analysis of off-grid and grid-connected power systems [16]. HOMER considers two economic indicators, Net Present Cost (NPC) and Levelized Cost Of Energy (LCOE). The total NPC of a system is the present value of all the costs the system incurs over its lifetime, minus the present value of all the revenue it earns over its lifetime. Costs include capital costs, replacement costs, O&M costs, fuel costs, emissions penalties, and the costs of buying power from the grid. Revenues include salvage value and grid sales revenue. HOMER calculates the total NPC by summing the total discounted cash flows in each year of the project lifetime [17]. The formula for calculating NPC is expressed as follows.

$$NPC = I + \sum_{i=1}^n (C_y) \left[\frac{1}{(1+d)^i} \right] \quad (34)$$

I : Initial capital cost [JPyen]

n : Project span [year]

C_y : Yearly cost (O&M and replacement) [JPyen]

d : Discount rate [%]

The LCOE is defined as the average cost per kWh of electrical energy produced by the system, as follows.

$$LCOE = \frac{C_{ann,tot}}{E_{served}} \quad (35)$$

E_{served} : Total electrical served [kWh/year]

$C_{ann,tot}$: Total annualized cost of the system [JPyen/year]

However, the LCOE provided by HOMER only considers the installation, maintenance, and replacement costs for each renewable energy system, and does not include the cost of electricity purchased from the power company. Therefore, in this study, we include the price of the total annual electricity supplied by the utility company in $C_{ann,tot}$, and calculate it as the Net Present Value (NPV) per year, which is used as the true $C_{ann,tot}$ in the calculation of LCOE.

Fig.54 represents the proposed grid-tied system, including solar PV, wind turbines, fuel cells, electrolyzers, and hydrogen tanks, as shown in the (FC: Fuel cell, WT: Wind turbine). All renewable energy systems are connected to the DC bus, and the electrolyzer uses only electricity supplied by solar and wind power to electrolyze water and produce hydrogen. The AC bus is connected only to the grid,

and the electricity provided by the power company is used solely for power consumption on campus.

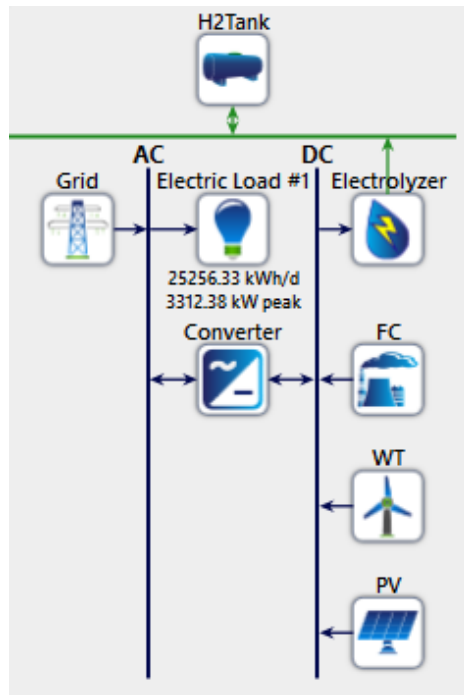


Fig. 54 HOMER simulation model

Fig.55 shows the average hourly power consumption, maximum and minimum power consumption for each month at Chikushi campus. When considered throughout the year, the average total daily power consumption is 25256 kWh/day, and the total annual power consumption is 9218.5 MWh/year.

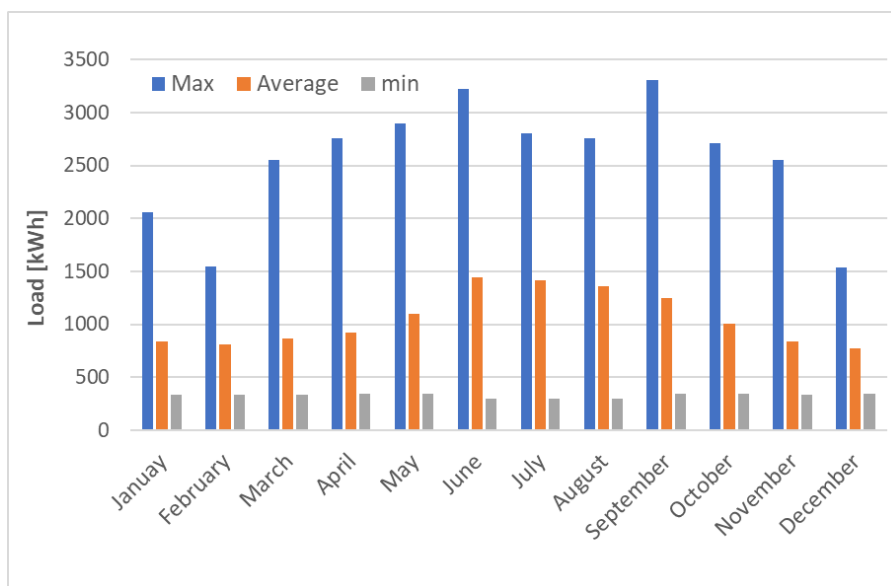


Fig. 55 Hourly power consumption in each month

The specifications of each component of the HRES shown are described below:

PV system: The technical details of the solar panels used in the HOMER simulation are as follows.

Table. 18 Specification of PV system [18]

Parameter	Value
Rated Power [kW]	1
Temperature coefficient [%/°C]	-0.258
Maximum efficiency [%]	21.7
Nominal operating cell temperature [°C]	44
Nominal operating ambient temperature [°C]	20
Incident radiation under test condition [W/m ²]	1000
Cell temperature under test condition [°C]	25
Derating factor [%]	90

Wind turbine: In this study, the wind turbine size is limited in the range of 0 to 10 kW. This is because the campus site area where the HRES will be installed is restricted, and wind turbines require more land than any other renewable energy system.

Hydrogen system: The installed capacity of the hydrogen system is considered as: 1kW (Fuel cell): 10kW (Electrolyzer): 1kg (H₂ tank). This is based on the assumption that the electrolyzer operates for 9 hours during the day to produce hydrogen, and the fuel cell consumes the stored hydrogen for 7 hours after sunset. For example, if the size of the fuel cell is 10 kW, the consumption of hydrogen is 0.275 kg/kWh. Therefore, the amount of hydrogen consumed by this fuel cell in a day can be obtained from the following equation.

$$0.275 \text{ [kg/kWh]} \times 10 \text{ [kWh]} \times 7 \text{ [hour]} = 19.25 \text{ [kg]} \quad (36)$$

From the above equation, a H₂ tank of about 20 kg is required. The electrolyzer's power consumption in this study is 46.4 [kWh] per 1 kg of hydrogen. The following equation gives the size of the electrolyzer required to produce 19.25 kg of hydrogen.

$$19.25 \text{ [kg]} \times 46.4 \text{ [kWh/kg]} / 9 \text{ [hour]} = 99.24 \text{ [kW]} \quad (37)$$

As the fuel cell size increases, the amount of hydrogen consumed per kWh of electricity generated increases. For a 100 kW fuel cell, which is the upper limit of this study, the value is about 0.29 [kg/kWh].

Table.19 shows the current estimated costs for each component and economic data. The costs are divided into initial capital cost, O&M cost, and replacement cost. In addition, the purchase price of electricity was considered to be 22 JPYen/kWh [20].

Table. 19 Costs of components and economic data

Component	Lifetime [years]	Initial capital cost [JPYen]	Replacement [JPYen]	O&M [JPYen/year]	Reference
PV [kW]	20	230,000	230,000	P&O:11,500 Fuzzy :10,924	[21]
WT [kW]	20	250,723	250,723	7,740	[22],[23]
Fuel cell [kW]	10	400,000	400,000	9,000	[21]
Electrolyzer [kW]	10	170,000	170,000	3,000	[21]
H ₂ tank [kg]	20	150,000	150,000	4,000	[21]
Inverter [kW]	20	13,970	13,970	110	[22]
Parameter	Values				
Nominal discount rate [%]	0.3				
Expected inflation rate [%]	0.98				
Project lifetime [years]	20				

In Table.19, different values of O&M cost for PV are shown for P&O and fuzzy controller. This is because the economic benefit from surplus power generated by the fuzzy controller is converted to a reduction in O&M cost. In solar PV, the fuzzy controller generated 26.2 kWh/kW more electricity per year than P&O, which brings savings of about 576 JPYen. This saving was deducted from the O&M cost of the P&O controller and used as the fuzzy O&M cost.

6.1 Base case scenario

The simulations were performed for 10 different fuel cell sizes from 10kW to 100kW at 10kW intervals. The capacity of each component, except the hydrogen system, is determined by HOMER optimization. The simulation results show that the best COE for both P&O and the fuzzy controller is obtained when the smallest fuel cell of 10 kW is used. Table.20 and 21 respectively show the breakdown of HRES and cost analysis results for a 10 kW fuel cell.

Table. 20 Component capacity and electricity production

	P&O		Fuzzy	
	Size [kW]	Electricity production [MWh/year]	Size [kW]	Electricity production [MWh/year]
PV	1675	2350	1782	2500
Wind turbine	10	14.5	10	14.5
Fuel cell	10	4.26	10	4.6
Electrolyzer	100	-54.1	100	-58.3
H₂ tank	20	—	20	—
Converter	1492	—	1542	—
Grid purchase	—	7253	—	7144

Table. 21 Cost Analysis Comparison of P&O and Fuzzy Controller

	NPC [JPYen]	COE [JPYen]	Operating cost [JPYen/year]	Total O&M [JPYen]	Initial capital [JPYen]
P&O	4.31B	38.09	180M	3.86B	433M
Fuzzy	4.29B	37.74	178M	3.81B	458M
Difference	21.4M	0.342	2.17M	46.7M	25.3M

Table.20 shows that the fuzzy model enables the installation of more PV systems than P&O. This can be attributed to the reduction of O&M cost with the benefit due to the fuzzy controller, resulting in the implementation of more solar panels. With the increase in PV system generation, the energy supply to the electrolyzer also increases. This means that the fuel cell in the fuzzy model generates more electricity than the one in the P&O. Furthermore, from Table.21, the fuzzy controller shows better cost-benefits. In particular, compared to P&O, the annual operating cost was reduced by about 2 million JPYen, and 47 million JPYen was reduced from the total O&M cost.

6.2 *Future cost scenario*

This section discusses the cost analysis of the HRES components based on their future prices. Table.22 summarizes the initial capital costs in 2020 and expected costs in 2030 for solar panels, wind turbines, fuel cells, and electrolyzers. Over the past few years, the amount of renewable energy installed has increased dramatically due to the policies, research and development, and funding of each major country. Among them, solar power is considered to be one of the most competitive technologies. According to Fig.56 the total installed cost decreased by 74% between 2010 and 2018. In wind power, improvements in technology and manufacturing processes, as well as the rise of competitive supply chains, are driving down the price of installation costs; average prices in 2018 ranged from 790 to 900USD/kW, down from 910 to 1050 USD/kW in 2017. In 2017, the Japanese government established the Strategic Roadmap for Hydrogen and Fuel Cells, the world's first national hydrogen strategy. Specifically, it aims to achieve hydrogen costs comparable to gasoline and LNG costs, along with a reduction in the cost of installing fuel cells and electrolysis equipment [24,25].

Based on the cost projections in Table.22, the following three scenarios were considered for the proposed FLC-based hybrid system.

- Scenario (1): future costs are only applied to solar panel
- Scenario (2): future costs are only applied to fuel cells and electrolyzers
- Scenario (3): Future costs are applied to all components

Table. 22 Summary of current and future initial capital costs

Component	2020 [JPYen]	2030 [JPYen]
PV [kW]	230,000	91,740 [22]
WT [kW]	250,723	187,000 [23]
Fuel cell [kW]	400,000	300,000 [24]
Electrolyzer [kW]	170,000	50,000 [24]

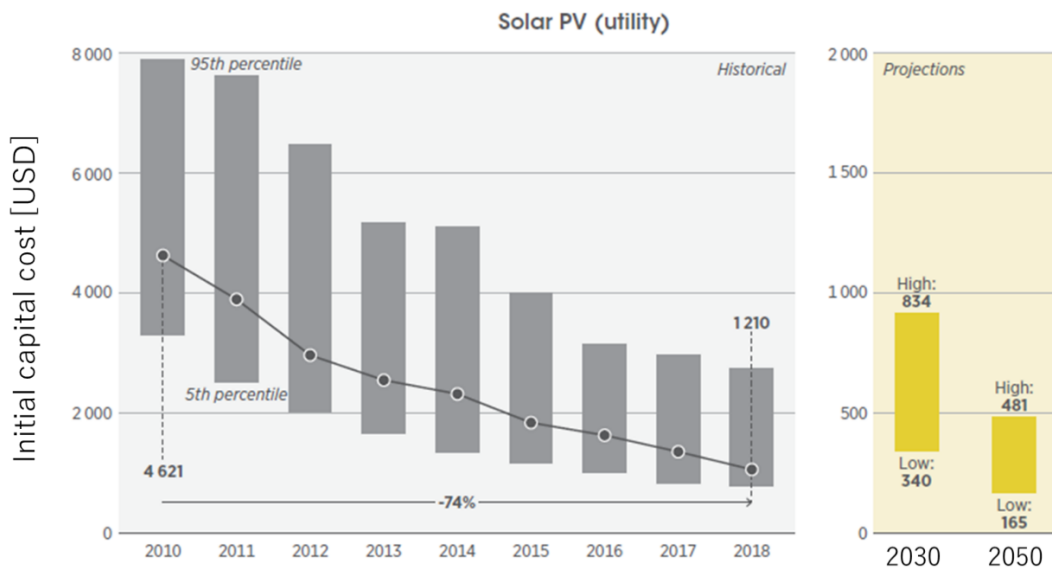


Fig. 56 Trends in initial capital cost of PV (Adapted from [22])

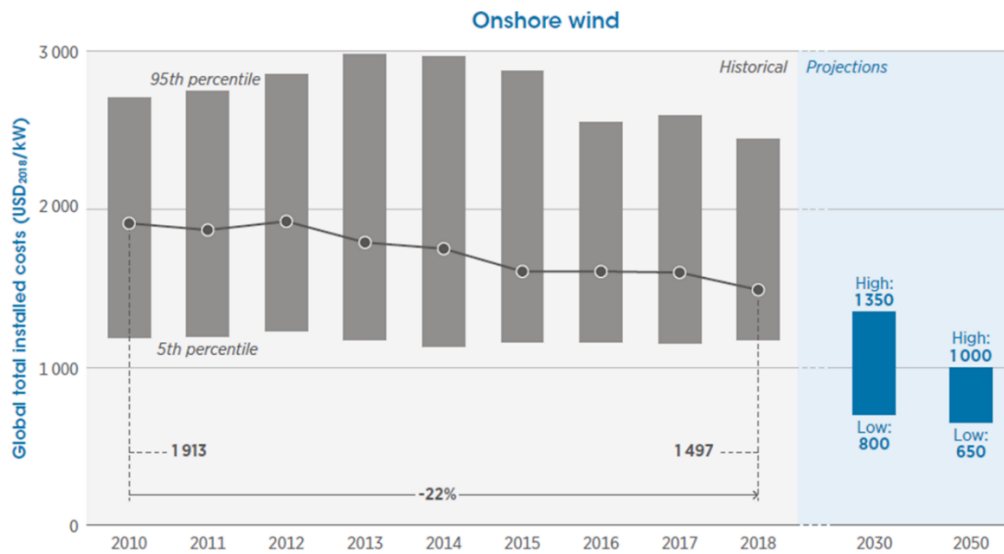


Fig. 57 Initial capital cost of Wind turbine (Adapted from [23])

Table.23 shows the respective COEs based on the above scenarios, taking into account the various sizes of the cells from 10 kW to 100 kW. The lowest COE can be achieved with a 10kW fuel cell in all scenarios. The best results are shown in scenario (3).

Table. 23 Summary of COE for each model

	Fuel cell size									
	10kW	20kW	30kW	40kW	50kW	60kW	70kW	80kW	90kW	100kW
Based on current cost [JPYen]	37.74 (A)	38.05	38.28	38.58	38.73	38.98	39.21	39.47	39.74	40.04
Scenario (1) [JPYen]	28.59 (B)	28.75	29.00	29.20	29.40	29.61	29.80	30.06	30.22	30.49
Scenario (2) [JPYen]	37.61 (C)	37.77	37.83	37.95	38.11	38.18	38.38	38.45	38.59	38.70
Scenario (3) [JPYen]	28.41	28.50	28.59	28.64	28.74	28.81	28.88	28.97	29.07	29.33 (D)

A: Base Scenario with 10 kW Fuel cell; B: Scenario (1) with 10 kW Fuel cell; Scenario (2) with 10 kW Fuel cell; Scenario (3) with 100 kW Fuel cell;

Table.24 shows the component sizes of each RES for different classes of (A) through (D). It can be seen that all the component sizes of class (C) are the same as the class (A), and there is not much difference in the COE, even though the installation cost of the hydrogen system is decreasing. This is because the hydrogen system is only powered by the PV system. As long as PV system installations do not increase due to falling PV panel installation costs, the amount of electricity generated by the fuel cell will not increase, and the share of HRES in the total electricity will not change. In addition, class (D) has the most extensive size of the hydrogen system and the largest solar panels to provide its electricity supply.

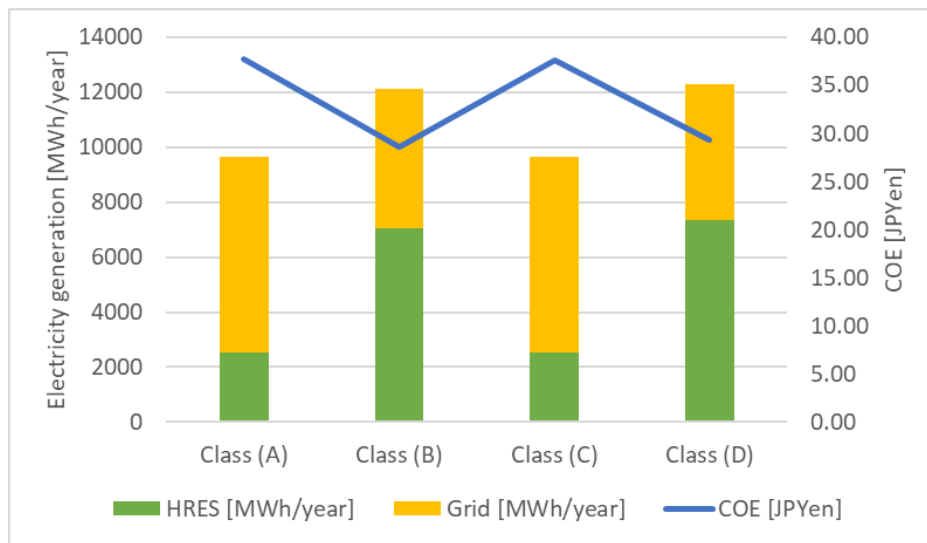
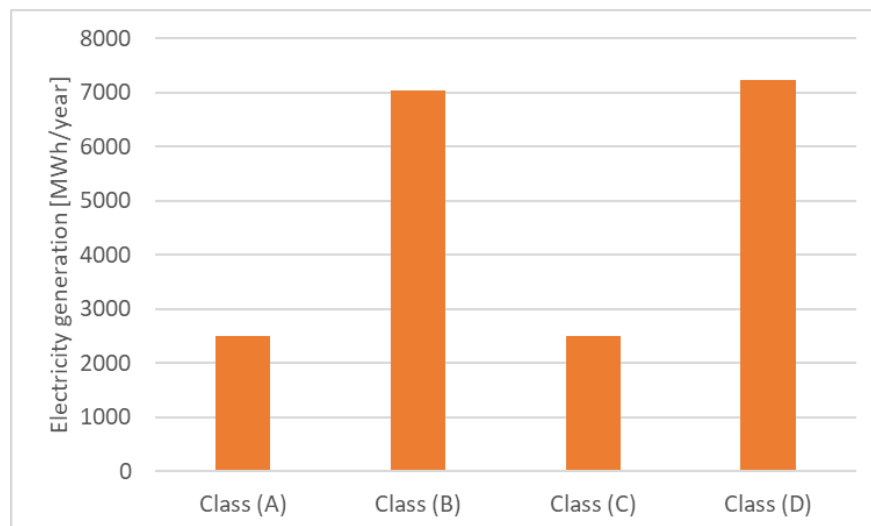
Table.25 shows the power generation and COE for each component from class (A) to class (D). Based on class (D), the amount of electricity generated by each component increases in proportion to the installed capacity shown in Table.24. Figures 60 to 62 show a graphical visualization of the contents of Table.25. Figure 60 shows the power generation of the PV system, wind turbine, and fuel cell in each model as a single HRES, together with the COE. Fig.58 to 60 show a graphical visualization of the contents of Table.25. Figure 58 shows the amount of output power from the PV system, wind turbine, and fuel cell for each class as a single HRES, along with the COE. Figures 59 and 60 show the amount of output power from the PV system and the fuel cell, separately. It can be observed from these figures that, the power generation from the fuel cell in (D) is substantial. Based on these results, larger capacity components can be adopted as the installation and maintenance costs of renewable energy systems are expected to be reduced in the future. This will lead to better COE, which will contribute to the realization of a cleaner energy society.

Table. 24 Size of each component of the HRES

	PV [kW]	Wind turbine [kW]	Fuel cell [kW]	Electrolyzer [kW]	H ₂ tank [kg]	Converter [kW]
Class (A)	1782	10	10	100	20	1542
Class (B)	5008	10	10	100	20	2786
Class (C)	1782	10	10	100	20	1542
Class (D)	5148	10	100	1000	200	2785

Table. 25 Power generation from each component of the HRES

	PV [MWh/year]	Wind turbine [MWh/year]	Fuel cell [MWh/year]	Grid [MWh/year]	COE [JPYen]
Class (A)	2500	14.5	4.6	7144	37.74
Class (B)	7026	14.5	14.3	5068	28.59
Class (C)	2500	14.5	4.6	7144	37.61
Class (D)	7223	14.5	114	4922	29.33

**Fig. 58 Electricity supply and COE for HRES and grid in each model****Fig. 59 Power generation of the PV system in each model**

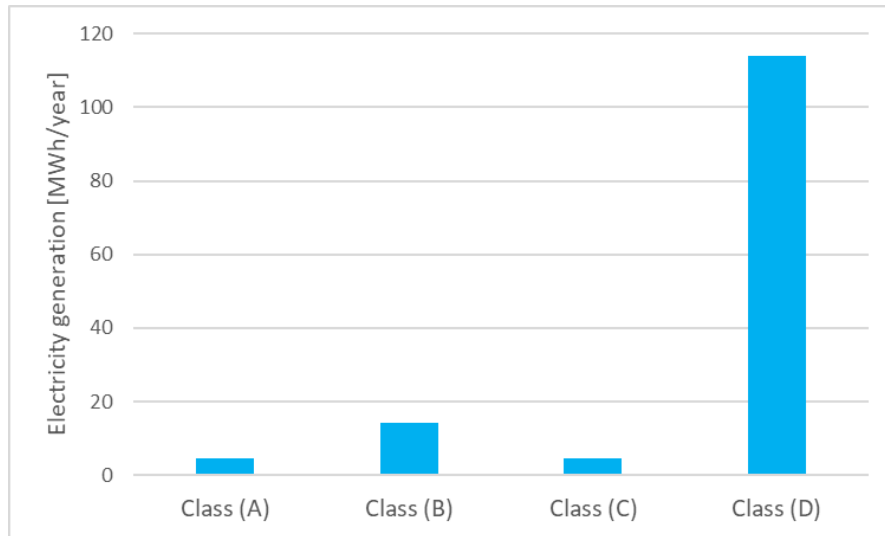


Fig. 60 Power generation of the Fuel cell in each model

Conclusion

In this study, techno-economic analysis of a grid-tied hybrid renewable energy system, which was supposed to be installed in the Chikushi campus of Kyushu University, was carried out. The HRES consists of three energy sources, PV, wind turbine generator, and fuel cell. Using a university campus as a case study, this thesis discussed the optimization of the HRES component sizes based on local climatic conditions, comparing and evaluating two MPPT technologies, P&O and fuzzy controller, and the cost evaluation of the system. This research has three main parts: 1) Measurement and collection of real data on solar radiation and cell temperature, 2) Implementation of a fuzzy logic controller, as an advanced MPPT system to realize the exact power point by converting ambiguous linguistic expressions used by humans, such as "large" and "small," into numerical values. Power generation simulations were conducted for both the new control system and the conventional P&O controller, and 3) Techno-economic analysis of implementing the proposed HRES in Chikushi campus, Kyushu University, using HOMER Pro to evaluate the cost of installing HRES and operating it for 20 years.

The techno-economic analysis of the proposed HRES was evaluated, considering the current and future market costs of renewable energy systems. The base scenario was defined based on the current market cost of renewable energy systems. The impact of the future costs of each component (Solar, Wind, Fuel Cell) of HRES in 2030 was evaluated in three scenarios: Scen (1): future costs were only applied to PV systems, Scen (2) : future costs were only applied to hydrogen systems, and Scen (3): future costs were applied to all components.

There is a significant difference in the COE between Scenarios (1) and (2). This is because the only energy source for the electrolyzer that supplies hydrogen to the fuel cell is the electricity generated by the PV system. Therefore, even if the installation cost of the hydrogen system alone decreases, if the cost of the PV system that supplies the energy to the hydrogen system remains the same, the capacity of the hydrogen system cannot be increased, and as a result, the COE will not change significantly. In other words, the cost of the solar system, which is the largest energy source in the HRES, is important for improving the COE. In addition, the cost analysis showed a significant decrease in COE is obtained, only when future costs are applied to all components. This study proves that larger systems can be installed if the costs of installing and maintaining renewable energy systems are reduced as expected. It is also expected that in the future, the price of electricity produced from renewable energy systems will be closer to the price of electricity generated from fossil fuels.

Reference

- [1] Agency for Natural Resources and Energy, Japan, JAPAN'S ENERGY 2019.
- [2] Roth, A., Boix, M., Gerbaud, V., Montastruc, L., & Etur, P. (2019). A flexible metamodel architecture for optimal design of hybrid renewable energy systems (HRES) – Case study of a stand-alone HRES for a factory in tropical island. *Journal of Cleaner Production*, 223, 214-225.
- [3] Alba Elena Garcia Alonso, Jesus Angel Oliver Ramires. (2017). Maximum power point tracking algorithms for solar photovoltaic.
- [4] Konrad Mertens. (2019). *Photovoltaics* (2nd ed.). WILEY.
- [5] Shaqour, A., Farzaneh, H., Yoshida, Y., & Hinokuma, T. (2020). Power control and simulation of a building integrated stand-alone hybrid PV-wind-battery system in Kasuga city, Japan. *Energy Reports*, 6, 1528-1544.
- [6] Tiwari, R., & Babu, N. R. (2016). Fuzzy logic based MPPT for permanent magnet synchronous generator in wind energy conversion system. *IFAC-PapersOnLine*, 49(1), 462-467.
- [7] Energy Chord:
http://energychord.com/children/energy/motor/sync/contents/sync_principle.html
- [8] Embedded Technology Lab.: <https://emb.macnica.co.jp/articles/1754/>
- [9] Ezinwanne, O., Zhongwen, F., & Zhijun, L. (2017). Energy performance and cost comparison of MPPT techniques for photovoltaics and other applications. *Energy Procedia*, 107, 297-303.
- [10] Anwasha Panigrahi, Kanhu Charan Bhuyan. (2017). Fuzzy Logic Based Maximum Power Point Tracking Algorithm for Photovoltaic Power Generation System. *Journal of Green Engineering*, 6(4), 403-426.
- [11] Stanford Encyclopedia of Philosophy: <https://plato.stanford.edu/entries/logic-fuzzy/>
- [12] Bendib, B., Krim, F., Belmili, H., Almi, M., & Boulouma, S. (2014). Advanced fuzzy MPPT controller for a stand-alone PV system. *Energy Procedia*, 50, 383-392.
- [13] Algarín, C. R., Fuentes, R. L., & Castro, A. O. (2018). Implementation of a cost-effective fuzzy MPPT controller on the Arduino board. *International Journal on Smart Sensing and Intelligent Systems*, 11(1), 1-10.
- [14] EKO website: https://eko.co.jp/products/solar_radiation_measurement/pyranometer/p1012.html
- [15] PV education: <https://www.pveducation.org/pvcdrom/modules-and-arrays/nominal-operating-cell-temperature>
- [16] Shahzad, M. K., Zahid, A., Ur Rashid, T., Rehan, M. A., Ali, M., & Ahmad, M. (2017). Techno-economic feasibility analysis of a solar-biomass off grid system for the electrification of remote rural areas in Pakistan using HOMER software. *Renewable Energy*, 106, 264-273.
- [17] HOMER website: <https://www.homerenergy.com/>
- [18] Panasonic, Panasonic Residential Catalog. Available online:
<https://sumai.panasonic.jp/catalog/solarsystem.html>
- [19] Takatsu, N., & Farzaneh, H. (2020). Techno-economic analysis of a novel hydrogen-based hybrid renewable energy system for both grid-tied and off-grid power supply in Japan: The case of Fukushima prefecture. *Applied Sciences*, 10(12), 4061.
- [20] Yoshida, Y., & Farzaneh, H. (2020). Optimal design of a stand-alone residential hybrid Microgrid system for enhancing renewable energy deployment in Japan. *Energies*, 13(7), 1737.
- [21] Sector VP. Wind Power. *Green Energy Technol* 2012;20:231–56.

[22] IRENA, FUTURE OF SOLAR PHOTOVOLTAIC

[23] IRENA, FUTURE OF WIND

[24] Agency for Natural Resources and Energy:

https://www.meti.go.jp/shingikai/energy_environment/suiso_nenryo/pdf/018_01_00.pdf

[25] Ministry of Economy, Trade and Industry:

https://www.meti.go.jp/shingikai/energy_environment/suiso_nenryo/pdf/018_01_00.pdf